This work is funded by the Department of Energy's Kansas City National
Security Campus, operated by Honeywell Federal Manufacturing &
Technologies, LLC, under contract number DE-NA0002839.

ADDITIVE MANUFACTURING OF REFRACTORY ALLOYS

by

Abigail Miklas

Unclassified Unlimited Release
NSC-614-4923, 11/2022

A thesis submitted to the Faculty and the Board of Trustees of the Colorado School of Mines in partial fulfillment of the requirements for the degree of Master of Science (Metallurgical and Materials Engineering).

Golden, Colorado
Date ________________________

Signed: ________________________________
Abigail Miklas

Signed: ________________________________
Dr. Amy Clarke
Thesis Advisor

Signed: ________________________________
Dr. Jonah Klemm-Toole
Thesis Advisor

Golden, Colorado
Date ________________________

Signed: ________________________________
Dr. Ivar Reimanis
Professor and Department Head
Metallurgical and Materials Engineering

ABSTRACT

Refractory alloys are known for their high temperature capabilities and are intended for use at ultra-high temperatures above even 1200°C, which exceeds the capabilities of conventional superalloys. Additive manufacturing (AM) is an attractive alternative processing route because refractory alloys are difficult to fabricate through traditional methods; AM can form a near net-shape part with a tailored microstructure. This work seeks to evaluate the solidification behavior of refractory alloys under AM conditions and establish corresponding solidification models. Two binary alloys, Mo30Nb and Nb7.5Ta, as well as the commercial Nb alloy, C103, and one refractory high entropy alloy (RHEA), MoNbTaTi, were subjected to single track melts in a laser powder bed fusion (LPBF) machine. Each melt track was evaluated in the scanning electron microscope (SEM), which determined that some AM conditions used led to non-ideal behavior. Electron backscatter diffraction (EBSD) revealed that the Nb7.5Ta, C103, and MoNbTaTi all exhibited new grain nucleation to various extents while the Mo30Nb exhibited primarily epitaxial growth. This was found to be inconsistent with solidification models that were developed for each alloy and each set of AM conditions to predict the columnar to equiaxed transition behavior (CET) of the experimental microstructures. This disparity was largely attributed to the input parameters for the solidification model, which were developed using Thermo-Calc and SYSWELD. These input parameters include the alloy specific Gibbs-Thomson coefficient and thermophysical properties, the solute specific liquidus slopes and partitioning coefficients, as well as the process specific thermal gradients. Each input parameter was evaluated to determine the likely changes required for the modeled values to generate solidification models that better correspond to what was observed experimentally.

TABLE OF CONTENTS

ABSTRACT........iii

LIST OF FIGURES........v

LIST OF TABLES........vii

ACKNOWLEDGEMENTS........viii

CHAPTER 1 INTRODUCTION........1

1.1 Objective........2

1.2 Background........2

1.3 References........4

CHAPTER 2 ADDITIVE MANUFACTURING FEASIBILITY OF REFRACTORY ALLOYS........7

2.1 Abstract........7

2.2 Introduction........7

2.3 Experimental Procedures........8

2.4 Results........14

2.5 Discussion........20

2.6 Conclusions........29

2.7 Acknowledgements........30

2.8 References........30

CHAPTER 3 SOLIDIFICATION BEHAVIOR OF REFRACTORY ALLOY C103 UNDER ADDITIVE MANUFACTURING CONDITIONS........35

3.1 Abstract........35

3.2 Introduction........35

3.3 Experimental Procedures........36

3.4 Results........42

3.5 Discussion........48

3.6 Conclusions........53

3.7 Acknowledgements........54

3.8 References........54

CHAPTER 4 CONCLUSIONS........58

4.1 Conclusions........58

4.2 Recommendations for Future Work........59

APPENDIX A........61

LIST OF FIGURES

Figure 2.1 Top-down macro images of the five melt tracks completed on samples of Mo30Nb (a.), Nb7.5 Ta (b.), and MoNbTaTi (c.). Each melt track is labelled 1-5 which correlates to parameters detailed in Table 2.2 10

Figure 2.2 CALPHAD property predictions of density (a.), specific heat (b.), and thermal conductivity (c.) of each alloy of interest. 10

Figure 2.3 Representative depiction of the locations of the thermal gradient and cooling rate measurements on the temperature contour map for MoNbTaTi melt track 4. The solid-liquid interface is equivalent to the grey-orange interface, indicated with the yellow arrow. This cutout shows the tail through the longitudinal center of the melt pool, traveling from left to right. 12

Figure 2.4 Top-down images of each melt track on MoNbTaTi are represented in a – e while the cross-sectional micrographs are shown in f – j. In these images, yellow arrows indicate cracking, red arrows indicate casting porosity, and blue arrows indicate balling. The IPF maps are shown in k – o with the corresponding laser parameters depicted to the left of the images and the IPF key is shown above the IPF maps. 15

Figure 2.5 Top-down images for melt track 3 on each material are shown in a – c, while the cross sections are shown in d – f and g – i. In these images, yellow arrows indicate cracking, red arrows indicate casting porosity, and blue arrows indicate balling. The IPF maps are shown in g – i. The corresponding alloy is indicated to the left of the images and the IPF key is shown above the IPF maps. 17

Figure 2.6 Scheil simulations for Mo30Nb, Nb7.5Ta, and MoNbTaTi are shown in a – c. The EDS line scans are also shown for these materials in d – f, respectively. The scans shown in d and f represent dendritic regions while e targeted grain boundaries. Interdendritic regions are indicated with red arrows while dendritic regions are indicated with yellow arrows in d and f. 18

Figure 2.7 Melt track-specific CET solidification maps for each track on MoNbTaTi 19

Figure 2.8 CET solidification maps for melt track 3 for Mo30Nb (a), Nb7.5 Ta (b), and MoNbTaTi (c). 20

Figure 2.9 A comparison of the total undercooling of each alloy 23

Figure 2.10 Backscatter image of track 1 in MoNbTaTi showing primary dendrites near the bottom of the melt pool. The yellow line indicates an example measurement area. 25

Figure 2.11 CALPHAD property predictions of density (a.), specific heat (b.), and thermal conductivity (c.) of each alloy of interest as well as pure Nb. 29

Figure 3.1 Top-down macro image of the five melt tracks completed on the C103 sample. Each melt track is labelled 1-5 which corresponds to parameters detailed in Table 3.2. 37

Figure 3.2 Locations of the thermal gradient and cooling rate measurements on the thermal contour map for melt track 5. The solid-liquid interface is represented by the grey-red interface, indicated with a yellow arrow. This is a longitudinal cross section that shows the melt pool traveling from left to right with measurements placed along the tail of the melt pool tail 39

Figure 3.3 Top-down images of each melt track are represented in a. – e., cross-sectional micrographs are shown in f. – j. and IPF maps are shown in k. – o. The corresponding melt track parameters are shown to the left of the images and the IPF map key is shown above the IPF maps. 43

Figure 3.4 Cross-sectional backscatter image (a.) and IPF map (b.) of the AM sample with the build direction going upward. 44

Figure 3.5 Scheil simulations for C103 (a.) and the EDS line scans for the bulk, as-cast material (b.) and AM sample (c.). The dendritic region in (b.) is indicated with a red arrow while the interdendritic is indicated with a yellow arrow. 45

Figure 3.6 CET solidification map for C103 including the process maps for each melt track and AM sample. 47

Figure 3.7 Backscatter image of track 3 showing primary dendrites near the bottom of the melt pool. The yellow line indicates an example measurement area. 50

Figure 3.8 Thermal conductivity for C103 and pure Nb modeled in Thermo-Calc, experimental data for C103, and the extrapolated curve for C103. 53

Figure A.1 Top-down images of each melt track on Mo30Nb are represented in a – e while the cross-sectional micrographs and IPF maps are shown in f – j and k – o, respectively. The corresponding laser parameters are shown to the left of the images and the IPF key is shown above the IPF maps. 61

Figure A.2 Top-down images of each melt track on Nb7.5Ta are represented in a – e while the cross-sectional micrographs and IPF maps are shown in f – j and k – o, respectively. The corresponding laser parameters are shown to the left of the images and the IPF key is shown above the IPF maps. 62

Figure A.3 Melt track-specific CET solidification maps for each track on Mo30Nb including the process maps for their respective melt tracks. 63

Figure A.4 Melt track-specific CET solidification maps for each track on Nb7.5Ta including the process maps for their respective melt tracks. 64

LIST OF TABLES

Table 2.1 Measured chemistry for each refractory alloy of interest, represented in weight percent......... 9

Table 2.2 Laser parameters used for each melt track on all samples depicted in Figure 2.1. 9

Table 2.3 Input parameters used for CET model.. 12

Table 2.4 Measured and simulated melt track widths and depths. 18

Table 2.5 Summary of the experimental and predicted grain morphology. 24

Table 2.6 Gibbs-Thomson coefficient minimum and maximum estimations with input parameters...... 25

Table 2.7 PDAS calculated with the Ni alloy and approximated Gibbs-Thomson coefficients and the measured PDAS for melt track 3.. 26

Table 3.1 Chemistry for as-cast C103, represented in weight percent, and measured using combustion for the C, inert gas fusion for the H, N, and O, and inductively coupled plasma (ICP) mass spectrometry for the remaining elements. 37

Table 3.2 Laser parameters used for each melt track shown in Figure 1 as well as the parameters used for the AM sample.. 38

Table 3.3 CALPHAD thermophysical property predictions used to create the SYSWELD material files. 39

Table 3.4 Modeled and estimated input parameters used for CET model.. 40

Table 3.5 Measured and simulated melt track widths and depths for each parameter set and the AM sample.. 46

Table 3.6 Summary of the experimental results and predicted results generated with both the Thermo-Calc modeled and extrapolated thermal conductivities.. 47

Table 3.7 Estimated minimum and maximum Gibbs-Thomson coefficient, including input parameters. 51

Table 3.8 Measured PDAS compared to the PDAS calculated with the literature and estimated Gibbs-Thomson coefficients. PDAS calculated using the Rosenthal model is also included............ 51

ACKNOWLEDGEMENTS

I would like to acknowledge the support of Amy Clarke and Jonah Klemm-Toole, committee members Andy Deal and Kester Clarke, as well as key contributors Noah Phillips, Cody Lough, Wes Everhart, and Andrew Kustas. Thank you to Noah Phillips and Allegheny Technologies Incorporated (ATI) for providing material and material data in support of this project. This work was funded by the Department of Energy's Kansas City National Security Campus (KSCNC) which is operated and managed by Honeywell Federal Manufacturing Technologies, LLC under contract number DE-NA0002839. Lab facilities at KCNSC, ATI, and Colorado School of Mines were used to support this work. This research used resources of the TESCAN S8252G RAMAN-SEM/FIB at the Colorado School of Mines which was acquired through the support of the National Science Foundation (DMR-1828454). I also appreciate the contributions of Alec Saville, Chris Jasien, Megan Le Corre, Zane Fisher, and Gabriel Thompson.

I would also like to thank my parents, brother, fiancé, and most importantly my dog for their support over the course of this project. I could not have done this without them.

CHAPTER 1

INTRODUCTION

Refractory alloys are high strength materials known for their high temperature capabilities. These alloys are of particular interest for the aerospace and defense industries because they allow higher temperatures to be accommodated than conventional Ni and Co based superalloys. They first rose to prominence in the 1950's, motivated by the high temperatures required for vehicles travelling to and from space [1]. They are being pursued as an attractive alternative alloy for use in applications such as turbine engines and hypersonics because their temperature capabilities will allow engines and flight vehicles to operate at higher temperatures, which is more efficient and allows faster speeds to be achieved [2].

Refractory alloys are typically cast then undergo thermomechanical processing to achieve the desired final shape and microstructure. This has proven to be an expensive process though as both conventional refractory alloys and RHEAs tend to suffer from low room temperature ductility and high oxygen affinity making them difficult to thermomechanically process through traditional methods [3]. Therefore, opportunity exists to develop production methods that would enable RHEAs to be used more readily in ultra-high temperature applications. Additive manufacturing (AM) is an attractive alternative processing pathway because it is capable of producing near-net shape parts with tailored microstructures that require little or no thermomechanical processing. AM can also be performed in an inert gas environment that mitigates oxidation [4].

In a study conducted on the Nb alloy, C103, an additively manufactured sample produced via laser powder bed fusion (LPBF) was evaluated metallographically and underwent mechanical testing. Micrographs of the as-built sample show an equiaxed structure in the plane perpendicular to the build direction and a columnar structure in the plane parallel to the build direction. This is consistent with typical microstructures produced via AM. The mechanical testing performed on the as-built material revealed that both its room temperature and elevated temperature tensile strengths exceeded that of wrought. The elongation was lower for the as-built material than for the wrought, but it remained within specification limits. The results of this study indicate that AM, specifically LPBF, is a feasible alternative processing pathway for refractory alloys [1].

Refractory high entropy alloys (RHEAs) are a specific class of refractory alloys that are of particular interest for hypersonic applications [2]. In contrast to conventional alloys that are based on a single constituent, high entropy alloys (HEAs) are based on multiple principal constituents. This effectively expands the useable area of the phase diagram and makes new composition spaces possible [5]. These unique compositions in turn lead to unique property combinations; several have shown a high strength combined with high ductility [6]. Increased interest and research in HEAs in the early 2000s created space to improve upon the already desirable properties of traditional refractory alloys by developing RHEA systems, which are defined as HEAs containing refractory alloys as their primary constituents. Despite their promising properties, refractory alloys, specifically RHEAs, are not yet widely used because they are difficult to manufacture through conventional methods [1].

1.1 Objective

The hypothesis addressed by this project posits that single laser track melts in refractory alloys are representative of the microstructure in completed AM builds and show that LPBF laser conditions can be manipulated to create a tailored microstructure, which can be predicted by solidification models. The following questions were developed to address this hypothesis.

1. *Can refractory alloy microstructures be controlled by laser conditions?*

   The response of the solidified microstructure to different laser conditions was examined by evaluating several single-track melts performed on samples of bulk refractory alloys with LPBF equipment. Four refractory alloys, Mo30Nb, Nb7.5Ta, C103, and MoNbTaTi, were observed in this study. C103 was selected to be evaluated because it is a commercially available refractory alloy. The other three alloys are not commercially available but exhibit small freezing ranges that are beneficial for solidification segregation. Each melt track on all four alloys was analyzed metallographically to characterize the morphology of the melt pool and microstructure.

2. *Can the solidification behavior of refractory alloys under AM conditions be modeled?*

   Solidification models are a valuable asset in achieving a tailored microstructure in refractory alloys because, when calibrated, they would allow material and process specific predictions to be made that would result in more intentional future experimentation. Solidification models for each alloy and process examined experimentally were therefore created in an attempt to achieve this calibrated model. Their final predictions were compared to the experimental results to assess the model's validity. Solidification segregation was also predicted and validated with experimental results.

3. *Is the behavior observed in a single-track representative of that observed in a completed build?*

   This same characterization was completed for a full AM build of one refractory alloy and compared to the corresponding single-track melts to assess the applicability of the single-track analysis to a full build.

1.2 Background

It is important to assess the effect that various AM conditions have on the melt pool morphology in refractory alloys to target a specific microstructure. AM conditions have been shown to affect the melt pool morphology in several studies conducted on Al, Ti, and Ni-alloys. For instance, in a study completed on an Al alloy with an LPBF system, it was found that the laser power had the greatest effect on melt pool depth while the laser scan speed had the greatest effect on melt pool width [7]. In a different study that evaluated several Ti alloys processed with identical conditions in an LPBF environment, it was determined that the total undercooling of the alloy was closely related to the amount of equiaxed grains observed; alloys with a small total undercooling did not exhibit an equiaxed structure [8]. The grain morphology was also found to be related to the laser parameters in a study completed on a Ni alloy. The laser conditions that created a higher energy density formed microstructures that exhibited more significant new grain nucleation [9]. While some conditions merely change the morphology of each melt pool, some can cause material defects that may result in a failure during use or failure in the build. For example, some laser conditions can create keyhole-mode laser melting, in which a deep melt pool is formed. This keyhole melting has been observed to create voids at the base of the melt pool in stainless steels, which can result in a non-conforming build [10].

Single laser track melt experimentation like that conducted in this study has been completed for pure Mo and W [11. A]. Surface cracking was observed in both studies and compared to the behavior observed in completed builds. In the pure Mo analysis, it was found that Mo-oxides formed during solidification and contributed to the grain boundary cracking observed in both the single laser track melt as well as the completed build. In the pure W analysis, the cracking was attributed to the high ductile-brittle transition temperature of W. Analysis of the grain structure in a completed build revealed that the cracks propagated along the solidified grain boundaries. The oxygen present in the W contributed to crack propagation along the grain boundaries.

The solidified microstructures of completed builds for pure Mo, pure W, and C103 have been evaluated in separate studies and found to be consistent with typical microstructures produced via AM; equiaxed in the plane perpendicular to the build direction and primarily columnar in the plane parallel to the build direction [12, 13]. The columnar structure is the result of the epitaxial growth that has been observed in single track studies conducted on pure W and W alloys [14]. A single study has not related the behavior of a completed refractory alloy build to the isolated behavior in the single laser track melts.

The RHEA system MoNbTaW is of particular interest for hypersonic applications and has been the subject of recent studies. The quaternary system has been used successfully in a variety of laser-based AM processes, including LPBF [15, 16]. Much of the experimental work has been focused on high throughput analysis of various composition within the MoNbTaW alloy space to identify desirable compositions. Analysis of the solidified microstructure has been compared with CALPHAD phase modeling, which was determined to be an accurate representation of experimental result. The favorability of a given composition has largely been measured with microstructural analysis and mechanical property measurements [17, 18]. The solidification behavior of the microstructure for this RHEA system under

LPBS conditions has not been studied in depth as it relates to laser parameters or related to single-track melts.

Solidification segregation modeling has been completed for refractory alloy systems like those being evaluated in this study. The segregation behavior in the NbTaV- (Ti, W) alloy system was predicted using Scheil simulations and measured using energy dispersive spectroscopy (EDS). It was found that the dendritic segregation behavior in the as-cast material aligned with the simulated segregation behavior [19]. In MoNbTaW, the segregation behavior was measured both in as-cast material and as-built material. Dendritic segregation was observed in the as-cast sample while none was able to be resolved in an LPBF-processed sample likely because any segregation was too fine to be resolved with the basic EDS system [20, 21]. This assumption aligns with similar experimentation completed on C103 where it was found that the fast solidification rate inherent to the LPBF process prevented micro-segregation [22].

The solidified microstructure under LPBF conditions has been successfully predicted for Ni-based superalloys and Al-alloys. The simplified form of the Kurz-Giovanola-Trivedi (KGT) dendrite growth model was used for both alloy groups to predict the columnar to equiaxed transition (CET) while heat transfer modeling was used to simulate the LPBF process [23, 24]. This solidification modeling method paired with heat transfer modeling completed in SYSWELD was utilized in this study. Heat transfer modeling has been conducted for Ti-alloys using SYSWELD thermomechanical simulation software [19]. The solidification modeling being completed in this study has the potential to eliminate much of the experimentation because a calibrated model can predict the contribution each constituent element makes to the total system, which serves as a guide in alloy selection [25].

The effectiveness of solidification modeling has been evaluated for both Ni and Al-alloys by comparing measured primary dendrite arm spacing (PDAS) to PDAS calculated with the results of the solidification model and heat transfer simulation. In that analysis, the average measured and calculated values were found to be 0.4 and 0.5 μm, respectively. The measured and calculated PDAS values are expected to differ by less than an order of magnitude in an accurate model [23]. This same method was employed to validate the models and simulations generated in this study.

1.3 References

[1] N. R. Philips, M. Carl, and N. J. Cunningham, "New opportunities in refractory alloys," *Metallurgical and Materials Transactions*, vol. 51, no. 7, pp. 3299–3310, 2020.

[2] Y.-Zheng Yang, J.-ling Yang, and D.-Ning Fang, "Research progress on thermal protection materials and structures of hypersonic vehicles," *Applied Mathematics and Mechanics*, vol. 29, no. 1, pp. 51–60, 2008.

[3] Y. Zhang and Q. Xing, “High entropy alloys: Manufacturing Routes,” *Encyclopedia of Materials: Metals and Alloys*, pp. 327–338, 2022.

[4] J. M. Torralba and M. Campos, “High entropy alloys manufactured by Additive Manufacturing,” *Metals*, vol. 10, no. 5, p. 639, 2020.

[5] B. S. Murty, J. W. Yeh, and S. Ranganathan, “Chapter 2 - High-Entropy Alloys: Basic Concepts,” in *High entropy alloys*, Butterworth-Heinemann, 2014.

[6] Y. F. Ye, Q. Wang, J. Lu, C. T. Liu, and Y. Yang, “High-entropy alloy: Challenges and prospects,” *Materials Today*, vol. 19, no. 6, pp. 349–362, 2016.

[7] Q. Guo, C. Zhao, M. Qu, L. Xiong, L. I. Escano, S. M. Hojjatzadeh, N. D. Parab, K. Fezzaa, W. Everhart, T. Sun, and L. Chen, “In-situ characterization and quantification of melt pool variation under constant input energy density in laser powder bed fusion additive manufacturing process,” *Additive Manufacturing*, vol. 28, pp. 600–609, 2019.

[8] Y.-Y. Zhu, H.-B. Tang, Z. Li, C. Xu, and B. He, “Solidification behavior and grain morphology of laser additive manufacturing titanium alloys,” *Journal of Alloys and Compounds*, vol. 777, pp. 712–716, 2019.

[9] N. Raghavan, B. C. Stump, P. Fernandez-Zelaia, M. M. Kirka, and S. Simunovic, “Influence of geometry on columnar to equiaxed transition during electron beam powder bed fusion of in718,” *Additive Manufacturing*, vol. 47, p. 102209, 2021.

[10] W. E. King, H. D. Barth, V. M. Castillo, G. F. Gallegos, J. W. Gibbs, D. E. Hahn, C. Kamath, and A. M. Rubenchik, “Observation of keyhole-mode laser melting in laser powder-bed fusion additive manufacturing,” *Journal of Materials Processing Technology*, vol. 214, no. 12, pp. 2915–2925, 2014.

[11] P. Rebesan, M. Ballan, M. Bonesso, A. Campagnolo, S. Corradetti, R. Dima, C. Gennari, G. A. Longo, S. Mancin, M. Manzolaro, G. Meneghetti, A. Pepato, E. Visconti, and M. Vedani, “Pure molybdenum manufactured by Laser Powder Bed Fusion: Thermal and mechanical characterization at room and high temperature,” *Additive Manufacturing*, vol. 47, p. 102277, 2021.

[12] J. Braun, L. Kaserer, J. Stajkovic, K.-H. Leitz, B. Tabernig, P. Singer, P. Leibenguth, C. Gspan, H. Kestler, and G. Leichtfried, “Molybdenum and tungsten manufactured by Selective Laser Melting: Analysis of defect structure and Solidification Mechanisms,” *International Journal of Refractory Metals and Hard Materials*, vol. 84, p. 104999, 2019.

[13] O. Mireles, O. Rodriguez, Y. Gao, and N. Philips, “Additive manufacture of refractory alloy C103 for propulsion applications,” *AIAA Propulsion and Energy 2020 Forum*, 2020

[14] A. Talignani, R. Seede, A. Whitt, S. Zheng, J. Ye, I. Karaman, M. M. Kirka, Y. Katoh, and Y. M. Wang, “A review on additive manufacturing of refractory tungsten and tungsten alloys,” *Additive Manufacturing*, vol. 58, p. 103009, 2022.

[15] H. Dobbelstein, M. Thiele, E. L. Gurevich, E. P. George, and A. Ostendorf, “Direct metal deposition of refractory high entropy alloy monbtaw,” *Physics Procedia*, vol. 83, pp. 624–633, 2016.

[16] A. Ostovari Moghaddam, N. A. Shaburova, M. N. Samodurova, A. Abdollahzadeh, and E. A. Trofimov, “Additive manufacturing of high entropy alloys: A practical review,” *Journal of Materials Science & Technology*, vol. 77, pp. 131–162, 2021.

[17] M. Moorehead, K. Bertsch, M. Niezgoda, C. Parkin, M. Elbakhshwan, K. Sridharan, C. Zhang, D. Thoma, and A. Couet, “High-throughput synthesis of mo-nb-ta-W high-entropy alloys via additive manufacturing,” *Materials & Design*, vol. 187, p. 108358, 2020.

[18] M. A. Melia, S. R. Whetten, R. Puckett, M. Jones, M. J. Heiden, N. Argibay, and A. B. Kustas, “High-throughput additive manufacturing and characterization of refractory high entropy alloys,” *Applied Materials Today*, vol. 19, p. 100560, 2020.

[19] H. W. Yao, J. W. Qiao, M. C. Gao, J. A. Hawk, S. G. Ma, H. F. Zhou, and Y. Zhang, “NbTaV-(Ti,W) refractory high-entropy alloys: Experiments and modeling,” *Materials Science and Engineering*, vol. 674, pp. 203–211, 2016.

[20] O. N. Senkov, G. B. Wilks, D. B. Miracle, C. P. Chuang, and P. K. Liaw, “Refractory high-entropy alloys,” *Intermetallics*, vol. 18, no. 9, pp. 1758–1765, 2010.

[21] H. Zhang, Y. Zhao, S. Huang, S. Zhu, F. Wang, and D. Li, “Manufacturing and analysis of high-performance refractory high-entropy alloy via selective laser melting (SLM),” *Materials*, vol. 12, no. 5, p. 720, 2019.

[22] P. Mohammadpour and A. B. Phillion, “Solidification microstructure selection maps for laser powder bed fusion of multicomponent alloys,” *IOP Conference Series: Materials Science and Engineering*, vol. 861, no. 1, p. 012005, 2020.

[23] S. Liu, H. Zhu, G. Peng, J. Yin, and X. Zeng, “Microstructure prediction of selective laser melting alsi10mg using finite element analysis,” *Materials & Design*, vol. 142, pp. 319–328, 2018.

[24] C. Jasien, A. Saville, C. G. Becker, J. Klemm-Toole, K. Fezzaa, T. Sun, T. Pollock, and A. J. Clarke, “In situ X-ray radiography and computational modeling to predict grain morphology in β-titanium during simulated additive manufacturing,” *Metals*, vol. 12, no. 7, p. 1217, 2022.

[25] W. Kurz, B. Giovanola, and R. Trivedi, “Theory of microstructural development during Rapid Solidification,” *Acta Metallurgica*, vol. 34, no. 5, pp. 823–830, 1986.

CHAPTER 2

ADDITIVE MANUFACTURING FEASIBILITY OF REFRACTORY ALLOYS

A. Miklas[1], A. Deal[2], C. Lough[3], N. Phillips[2], A. Kustas[2], J. Klemm-Toole[4], A.J. Clarke[4]

2.1 Abstract

Refractory alloys are known for their high temperature capabilities and are often intended for use at ultra-high temperatures above 1200°C, which exceeds the capabilities of conventional Ni- and Co-based superalloys. Additive manufacturing (AM) is an attractive alternative processing route because refractory alloys are difficult to fabricate through traditional methods; AM can form a near net-shape part with a tailored microstructure. This work seeks to evaluate the solidification behavior of refractory alloys under AM conditions and establish corresponding solidification models. Two binary alloys, Mo30Nb and Nb7.5Ta, as well as one refractory high entropy alloy (RHEA), MoNbTaTi, were subjected to single track melts in a laser powder bed fusion (LPBF) machine. Each melt track was evaluated in the scanning electron microscope (SEM), which determined that some AM conditions led to deleterious keyholing or balling. Electron backscatter diffraction (EBSD) revealed that the Nb7.5Ta and MoNbTaTi both exhibited new grain nucleation while the Mo30Nb exhibited primarily epitaxial growth. This was found to be inconsistent with solidification models that were developed for each alloy and each set of AM conditions to predict the columnar to equiaxed transition behavior (CET) of the experimental microstructures. Several of the input parameters for the solidification models (i.e., Gibbs-Thomson coefficient, liquidus slope, partitioning coefficient, thermophysical properties, thermal gradient) were developed using Thermo-Calc and SYSWELD. The accuracy of these modeled values effect of associated input variable sensitivities on the solidification model predictions are discussed.

2.2 Introduction

Refractory alloys are known for their high temperature capabilities. They are generally intended for use at temperatures above 1200°C, which exceeds the capabilities of conventional Ni- and Co- based superalloys. These ultra-high temperature capabilities make refractory alloys particularly appealing for the aerospace and energy industry. The initial interest in refractory alloys and push for research in this area came in the 1950s to improve the capabilities of turbine engines; engines are more efficient the hotter they operate, so the temperature capabilities of the components become the limiting factor as the engine becomes more mechanically efficient [1]. Refractory alloys are still of interest today as the aerospace

---

[1] Author, performed most experimental work, participated in research planning

[2] Coauthor, helped with planning experiments and discussing results

[3] Performed single-track melts

[4] Project advisor, helped with planning experiments and discussing results

industry continues to push the temperature capabilities of components. Refractory high entropy alloys (RHEAs) are of particular interest for hypersonic applications [2]. In contrast to conventional alloys with a base element, high entropy alloys (HEAs) contain multiple principal elements. This effectively expands the useable area of the phase diagram and makes new composition spaces possible [3]. These unique compositions in turn lead to unique structure-property relationships; several have shown high strength combined with high ductility and exceptional temperature resiliency [4]. Increased interest and research in HEAs in the early 2000s created space to improve upon the already desirable properties of traditional refractory alloys by developing RHEAs. Despite their promising properties, refractory alloys, specifically RHEAs, are not yet widely used because they are difficult to manufacture through conventional methods [1].

Refractory alloys are typically cast, and then undergo thermomechanical processing to achieve the desired final shape and microstructure. This has proven to be an expensive process, as both conventional refractory alloys and RHEAs tend to suffer from low room temperature ductility in the as-cast state and high oxygen affinity making them difficult to thermomechanically process through traditional methods [5]. Therefore, opportunity exists to develop production methods that would enable RHEAs to be used more readily in ultra-high temperature applications. Additive manufacturing (AM) is an attractive alternative processing pathway because it can produce near-net shape parts with tailored microstructures that require little or no thermomechanical processing. AM can also be performed in an inert gas environment that mitigates oxidation [6].

To understand how to achieve a tailored microstructure, the solidification behavior of refractory alloys under AM conditions must be evaluated. This behavior was isolated in this work by performing single-track laser melts on samples of bulk refractory alloys with AM equipment. The melt tracks can be evaluated to determine the morphology of the melt pools and microstructures produced by different laser conditions to create guidelines to achieve desired microstructures.

Material modeling and heat transfer simulations can also be a useful tool to avoid lengthy build trials and metallographic analyses. However, before they can be used to predict solidification behavior, they must be validated with some experimentation. The single-track laser melt experimentation was used to validate models that describe the behavior of refractory alloys under AM conditions in this work.

2.3 Experimental Procedures

Three body-centered cubic refractory alloys were selected for evaluation: Mo30Nb, Nb7.5Ta, and MoNbTaTi. The compositions measured via inductively coupled plasma (ICP) mass spectrometry, ICP atomic emission spectroscopy, combustion, and inert gas fusion are represented in weight percent in Table 2.1.

Table 2.1: Measured chemistry for each refractory alloy of interest, represented in weight percent.

Element	Mo30Nb	Nb7.5a	MoNbTaTi
C	< 0.01	< 0.002	< 0.01
H	0.001	< 0.0003	0.001
Mo	69.71	< 0.0015	22.34
N	0.10	< 0.001	< 0.01
Nb	30.19	92.29	21.39
O	< 0.01	< 0.004	0.01
Ta	< 0.01	7.70	44.47
Ti	< 0.01	< 0.0025	10.93

The Mo30Nb and MoNbTaTi were evaluated in the as-cast condition while the Nb7.5Ta was fully recrystallized wrought material; each material had an average grain size of approximately 270 μm, 140μm, and 8 μm, respectively. Samples of each alloy were sectioned from bulk material and ground to be flat and parallel. The finished surface was ground with 1200-grit sandpaper to prepare the surface for the laser track melts. Five laser track melts were performed on each sample at the Kansas City National Security Campus (KCNSC) on their custom IPG Photonics AM-RAD Laser Powder Bed Fusion (LPBF) machine, equipped with an IPG Photonics YLR-500 fiber laser, in an argon gas environment with less than 200 ppm oxygen using the parameters shown in Table 2.2. the laser track melts were performed transverse to the rolling direction for the Nb7.5Ta. Different combinations of laser powers and speeds were used for each of the five melts to vary the melt pool morphology. These parameters were developed in a separate, internal study conducted by KCNSC and were found to produce ideal behavior in some refractory alloys. The location of the five melts on each sample is shown in Figure 2.1.

Table 2.2: Laser parameters used for each melt track on all samples depicted in Figure 2.1.

Parameter Set	Power [W]	Speed [m/s]	Beam Diameter [μm]	Linear Energy Density [J/m]
1	162	0.8	75	203
2	243	0.2	75	1215
3	162	0.5	75	324
4	405	1.7	75	238
5	324	1.7	75	191

All samples were evaluated in the as-received condition with no post-processing after the melt tracks were performed. The melt tracks were imaged in the top-down orientation using an Everhart-Thornley detector (ETD). The samples were sectioned close to the middle of the tracks where steady-state conditions could be assumed and the cross sections were prepared metallographically. Each melt track was imaged in the SEM and characterized with electron backscatter diffraction (EBSD). Both the melt tracks and the base material were evaluated with energy dispersive spectroscopy (EDS). Imaging and EDS measurements were taken in a TESCAN S8000G scanning electron microscope (SEM) equipped with an EDAX Octane Elect Plus EDS system using beam currents ranging from 300 pA - 10 nA, accelerating voltages ranging from 10 kV – 25 kV, and a working distance of 6 mm. EBSD characterization was completed in an FEI Helios NanoLab 600i SEM outfitted with an EDAX Hikari Super 1400pps EBSD detector using a beam current of 11 nA, accelerating voltage of 20 kV, and working distance of approximately 26 mm. Solidification segregation behavior was predicted by completing Scheil simulations in Themo-Calc using the TCHEA5 database to compare with the EDS results [7].

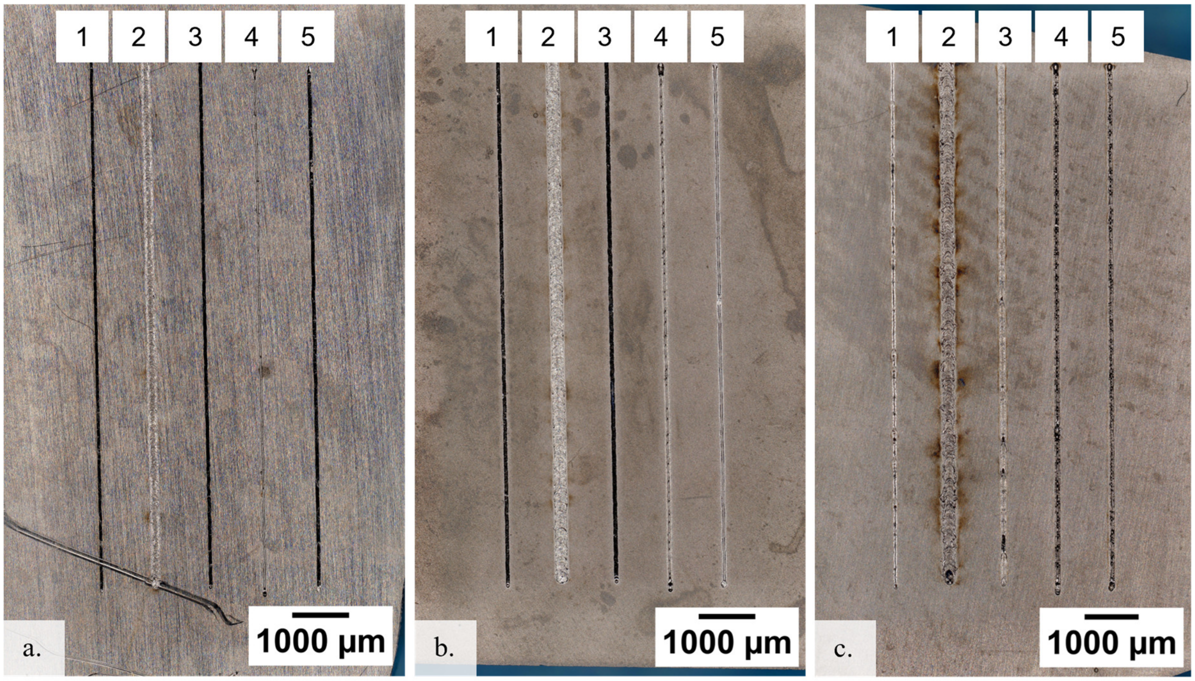

Figure 2.1. Top-down macro images were taken of the five melt tracks completed on samples of Mo30Nb (a.), Nb7.5 Ta (b.), and MoNbTaTi (c.). Each melt track is labelled 1-5 which correlates to parameters in Table 2.2.

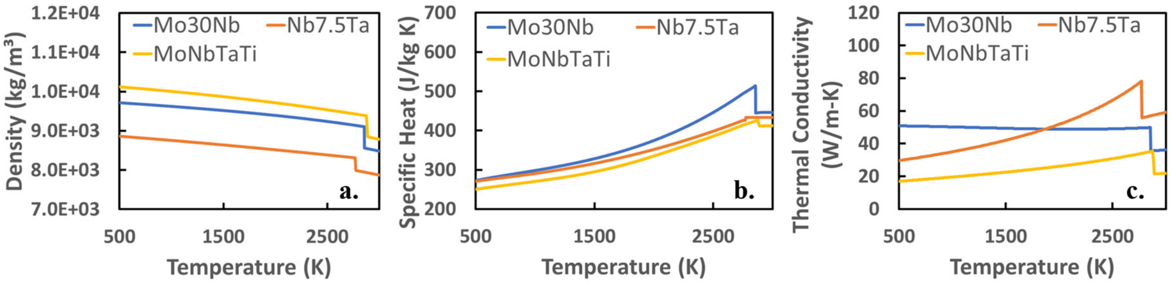

Figure 2.2. CALPHAD property predictions of density (a.), specific heat (b.), and thermal conductivity (c.) of each alloy of interest.

A commercial thermomechanical simulation software, SYSWELD, was used to simulate the heat transfer conditions of the single-track melts. Only conductive heat transfer was considered in the melt pool. Temperature fields from the heat transfer simulations were used to calculate the thermal gradient for each material and laser condition combination, which was used to create process curves for each experimental melt track. To create the required SYSWELD material files for the refractory alloys, the density, thermal conductivity, and specific heat for each alloy were modeled as functions of temperature in Thermo-Calc using the TCHEA5 database, Figure 2.2. Each property exhibited an abrupt change at the liquidus temperature.

Each alloy and laser condition combination were modeled using the experimental laser parameters to match the melt pool shape and size to what was measured in the cross sections. A maximum of approximately 10% difference between the experimental and modeled melt pool width and depth was targeted. The laser efficiency and load area were the input variables adjusted to achieve the target melt pool shapes and sizes. The temperature gradient at the solid-liquid interface was calculated at approximately five points of interest along each interface between the top and bottom of the melt pool, along the tail, as illustrated in Figure 2.3. This was accomplished using Equation 2.1 where G_x, G_y, and G_z are the thermal gradients at the solid-liquid interface in the x, y, and z directions while G is the total gradient at the solid-liquid interface. The directional temperature gradients were calculated using the temperatures generated by SYSWELD at each point of interest as well as the temperature one grid space away from the point of interest in each axial direction.

$$\mathrm{G} = \sqrt{\mathrm{G}_\mathrm{x}^2 + \mathrm{G}_\mathrm{y}^2 + \mathrm{G}_\mathrm{z}^2} \tag{2.1}$$

The corresponding solidification velocities V, are calculated for each point using the total thermal gradient and cooling rate $\dot{\mathrm{C}}$, which was generated by SYSWELD at each point of interest, in Equation 2.2. The solidification velocities are plotted as a function of thermal gradient to create process curves [8].

$$\mathrm{V} = \frac{\dot{\mathrm{C}}}{\mathrm{G}} \tag{2.2}$$

Alloy-specific solidification maps were developed for each alloy of interest to model the columnar to equiaxed transition (CET). Combining these with the heat transfer simulation allows the final microstructure to be predicted for each alloy and laser condition combination as fully columnar, fully equiaxed, or mixed microstructure. The CET models were created using the simplified form of the Kurz-Giovanola-Trivedi (KGT) dendrite growth model [9]. The key input variables for this model are solute diffusivities in the liquid $\mathrm{D_i}$, partitioning coefficients $\mathrm{k_i}$, liquidus slopes $\mathrm{m_i}$, Gibbs-Thomson coefficient Γ, and initial liquid solute concentration $\mathrm{C_0}$. In this simplified model, the solute diffusivities, partitioning coefficients, and liquidus slopes were assumed to be constant. The partitioning coefficients and liquidus slopes were modeled in Thermo-Calc using the TCHEA5 database while the Gibbs-Thomson coefficient and solute diffusivities were found in literature [10, 11]. Experimental values for Ni and Ti-alloys were used for the Gibbs-Thomson coefficient and diffusivity, respectively, based on the currently available experimental data. These were assumed to be an adequate substitution for unavailable refractory alloy values because both Ni and Ti-alloys have similar high temperature capabilities. The initial liquid solute concentration is inherent in the alloy composition. The input parameters used for each alloy are shown in Table 2.3.

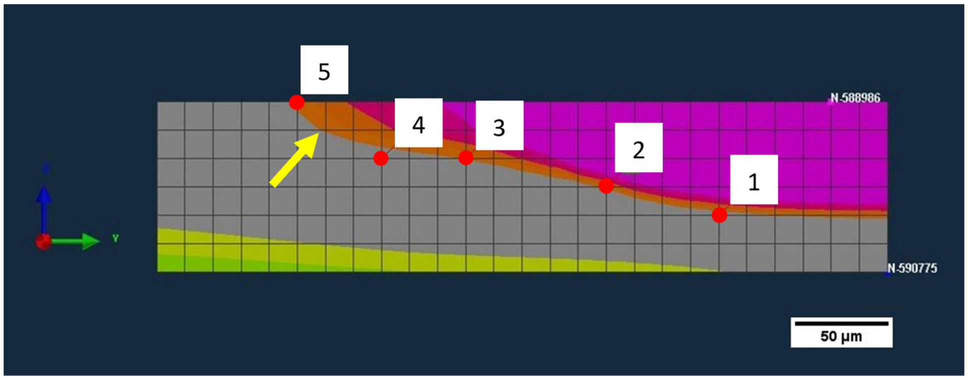

Figure 2.3. Representative depiction of the locations of the thermal gradient and cooling rate measurements on the temperature contour map for MoNbTaTi melt track 4. The solid-liquid interface is located the grey-orange interface, indicated with the yellow arrow. The orange, red, and pink colors indicate areas of liquid while grey and green indicate areas of solid. This cutout shows the tail through the longitudinal center of the melt pool, traveling from left to right.

Table 2.3: Input parameters used for CET model.

Alloy	Solute	Parameter	Value
Mo30Nb		Gibbs-Thomson Coefficient **[10]**	1.92E-7 K*m
	Nb	Diffusion Coefficient **[11]**	2.00E-9 m^2/s
		Partition Coefficient	0.97 mol/mol
		Liquidus Slope	-1.45 K/wt.%
		Initial Concentration	30.0 wt.%
Nb7.5Ta		Gibbs-Thomson Coefficient **[10]**	1.92E-7 K*m
	Ta	Diffusion Coefficient **[11]**	2.00E-9 m^2/s
		Partition Coefficient	1.26 mol/mol
		Liquidus Slope	4.08 K/wt.%
		Initial Concentration	7.5 wt.%
MoNbTaTi		Gibbs-Thomson Coefficient **[10]**	1.92E-7 K*m
	Mo	Diffusion Coefficient **[11]**	2.00E-9 m^2/s
		Partition Coefficient	1.04 mol/mol
		Liquidus Slope	6.03 K/wt.%
		Initial Concentration	23.0 wt.%
	Nb	Diffusion Coefficient **[11]**	2.00E-9 m^2/s
		Partition Coefficient	0.95 mol/mol
		Liquidus Slope	-0.09 K/wt.%
		Initial Concentration	22.2 wt.%
	Ti	Diffusion Coefficient **[11]**	2.00E-9 m^2/s
		Partition Coefficient	0.88 mol/mol
		Liquidus Slope	-4.45 K/wt.%
		Initial Concentration	11.5 wt.%

The equations used to create the G-V CET curves are described in Equations 2.3 – 2.9. Equation 2.3 is used to calculate the Peclet number, P_i, which is later used along with tip radius, R, and diffusion coefficient to calculate the solidification velocity, V, in Equation 2.8 [9]. The Peclet number is a function of the fluid velocity, v_i, the characteristic length of the system, L_i, and the diffusion coefficient [12]. The tip radius, R, is calculated in Equation 2.7, where the liquid solute concentration at the dendrite tip, C_i^*, is calculated with Equation 2.4, the Peclet number is calculated with equation 2.3, ξ_i is calculated with Equation 2.6, and G is the solidification thermal gradient [9, 10]. The Ivantsov function, $Iv(P_i)$, which is used in Equation 2.4 to calculate C_i^*, is shown in Equation 2.5, where E_1 is the exponential integral. Equations 2.9, 2.10, and 2.11 are used to calculate the solute undercooling, $\Delta T_{c,i}$, the dendrite tip curvature, ΔT_r, and the total undercooling, ΔT_{total}, respectively.

$$P_i = \frac{L_i v_i}{D_i} \tag{2.3}$$

$$C_i^* = \frac{C_o}{1 - [(1 - k_i) Iv(P_i)]} \tag{2.4}$$

$$Iv(P_i) = P_i e^{P_i} * E_1(P_i) \tag{2.5}$$

$$\xi_i = 1 - \frac{2k_i}{\sqrt{1 + \left(\frac{2\pi}{P_i}\right)^2} - 1 + 2k_i} \tag{2.6}$$

$$4\pi^2 \Gamma \left(\frac{1}{R^2}\right) + \left(2 \sum [m_i P_i (1 - k_i) C_i^* \xi_i]\right) \left(\frac{1}{R}\right) + G = 0 \tag{2.7}$$

$$V = \frac{2 P_i D_i}{R} \tag{2.8}$$

$$\Delta T_{c,i} = m_i (C_o - C_i^*) \tag{2.9}$$

$$\Delta T_r = \frac{2\Gamma}{R} \tag{2.10}$$

$$\Delta T_{total} = \sum_i \Delta T_{c,i} + \Delta T_r \tag{2.11}$$

The modeled solute undercooling, the curvature, and the total undercooling were plotted as functions of solidification velocity to show both total undercooling for the alloy as well as undercooling for each individual constituent, which can be useful in guiding future alloy compositions.

The total undercooling curve can be fit with a power law model, Equation 2.12, to determine the material constants a and n in Equation 2.13. This allows G to be calculated and complete the CET model. In Equation 2.13, N_o is the nucleation site density, ΔT_n is the nucleation undercooling, and Φ is the

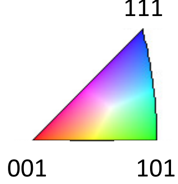

volume fraction of equiaxed grains, which is assigned a value of either 0.0066 and 0.49 to designate 1% or 50% equiaxed, respectively, which is conventional in CET modeling [13]. The nucleation site density and nucleation undercooling for a Ni-alloy were used to complete this model due to data availability for refractory alloys [14]. The high temperature capabilities of Ni-alloys that are like those of refractory alloys made these values an acceptable estimation.

$$\Delta T_{total} = (a * V)^{1/n} \tag{2.12}$$

$$G = \frac{1}{n+1} * \left(\frac{-4\pi N_o}{3\,ln(1-\Phi)}\right)^{\frac{1}{3}} * \left(1 - \frac{{\Delta T_n}^{n+1}}{(a*V)^{\frac{n}{n+1}}}\right) * (a*V)^{\frac{1}{n}} \tag{2.13}$$

The CET model is conventionally made up of two curves: one representing a microstructure with 1% equiaxed grains and one representing a microstructure with 50% equiaxed grains. An equiaxed structure is predicted when the Gs and Vs are above the 50% equiaxed line and a columnar structure is predicted when the Gs and Vs are below the 1% equiaxed line. However, even when a fully equiaxed structure is predicted, the grains will likely display some degree of elongation due to the large positive thermal gradient that is present during the solidification process.

2.4 Results

Top-down imaging was completed to characterize the melt track behavior. The images of the MoNbTaTi sample showing the behavior of each melt track are included in Figure 2.4 and were taken with the melt track running from left to right. All five melt tracks in the MoNbTaTi displayed cracking in the surface within the melt track and in the surrounding area, indicated with yellow arrows in Figures 2.4a – e. The cracks were primarily transverse to the melt track in tracks 1, 3, 4, and 5 (Figures 2.4a, c, d, and e, respectively), but were also longitudinal in melt track 2, as shown in Figure 2.4b. The transverse cracks extended into the base material and traveled along grain boundaries, indicated in the cross-sectional images in Figures 2.4f – j with yellow arrows. The cross-sectional images revealed casting porosity in the base material, indicated with red arrows, that are the result of solidification shrinkage [15, 16].

Figure 2.4. Top-down images of each melt track on MoNbTaTi are represented in a – e while the cross-sectional micrographs are shown in f – j. In these images, yellow arrows indicate cracking, red arrows indicate casting porosity, and blue arrows indicate balling. The IPF maps are shown in k – o with the corresponding laser parameters depicted to the left of the images and the IPF key is shown above the IPF maps.

The melt pools are outlined in a dashed yellow line in Figures 2.4f – j so the size and morphology of each track can be compared and related to the laser parameters used. Tracks 1 and 3 exhibited similar melt pool morphologies because they were created with the same laser power. Track 3 is slightly wider and deeper than track 1 because it used a slower scan speed and therefore a higher linear energy density.

Track 2 was created with the highest linear energy density, which produced the widest and deepest of all five tracks. The melt pool of track 2 was also the only track to exhibit keyholing behavior. Tracks 4 and 5 exhibited balling, indicated with blue arrows. Both were created with the highest speed. Because track 4 utilized a higher linear energy density than track 5, it was wider and deeper. These observations of the relative melt track behavior are similar for the Mo30Nb and Nb7.5Ta.

The inverse pole figures (IPF) maps created via EBSD of the MoNbTaTi in Figures 2.4k – o reveal epitaxial growth as well as new grain nucleation in all melt tracks. Track 1 displayed the least amount of new grain nucleation while track 2 displayed the highest amount of new grain nucleation. Although track 3 appeared to exhibit similar melt pool morphology to track 1 in the top-down and cross-sectional imaging, its higher linear energy density led to more new grain nucleation. Tracks 4, which was created with a higher linear energy density than track 5, displayed a higher amount of new grain nucleation than track 5.

All samples were imaged in the top-down orientation again after a light polish to evaluate any effect the dendritic structure in the base metal might have on the behavior of the melt track. It was determined that the dendritic structure and the resultant solidification segregation had no effect on the melt tracks for any alloys.

The top-down images, images of the polished cross sections, and the IPF maps of melt track 3 for each alloy are compared in Figure 2.5. Cracking similar to that observed in MoNbTaTi is also observed in Mo30Nb, but no cracking was observed in the Nb7.5Ta. The cross-sectional images of each melt track are shown in Figures 2.5d – f with each melt pool outlined with a dashed yellow line. The grain boundary cracking observed in the top-down orientation for the Mo-containing alloys was also present below the surface around the melt tracks. The IPF maps of melt track 3 for each alloy are shown in Figures 2.5g – i. The Nb7.5Ta and MoNbTaTi exhibited epitaxial growth as well as new grain nucleation within each track,, but the Mo30Nb only exhibited epitaxial growth.

The solidification segregation was predicted for each alloy using Scheil simulations, which are shown in Figure 2.6a – c. Across all three alloys, it was predicted that, when present, the Nb and Ti will segregate to the last solid to form (i.e., interdendritic regions) while the Mo and Ta will segregate to the first solid to form (i.e., dendritic regions). This behavior was expected because Mo and Ta have the two highest melting points and will therefore be the first to solidify. The Scheil simulations also predict the severity of the segregation that will occur in each alloy. These simulations indicate that the segregation will be the most severe in the MoNbTaTi and less significant in the Mo30Nb and the Nb7.5Ta.

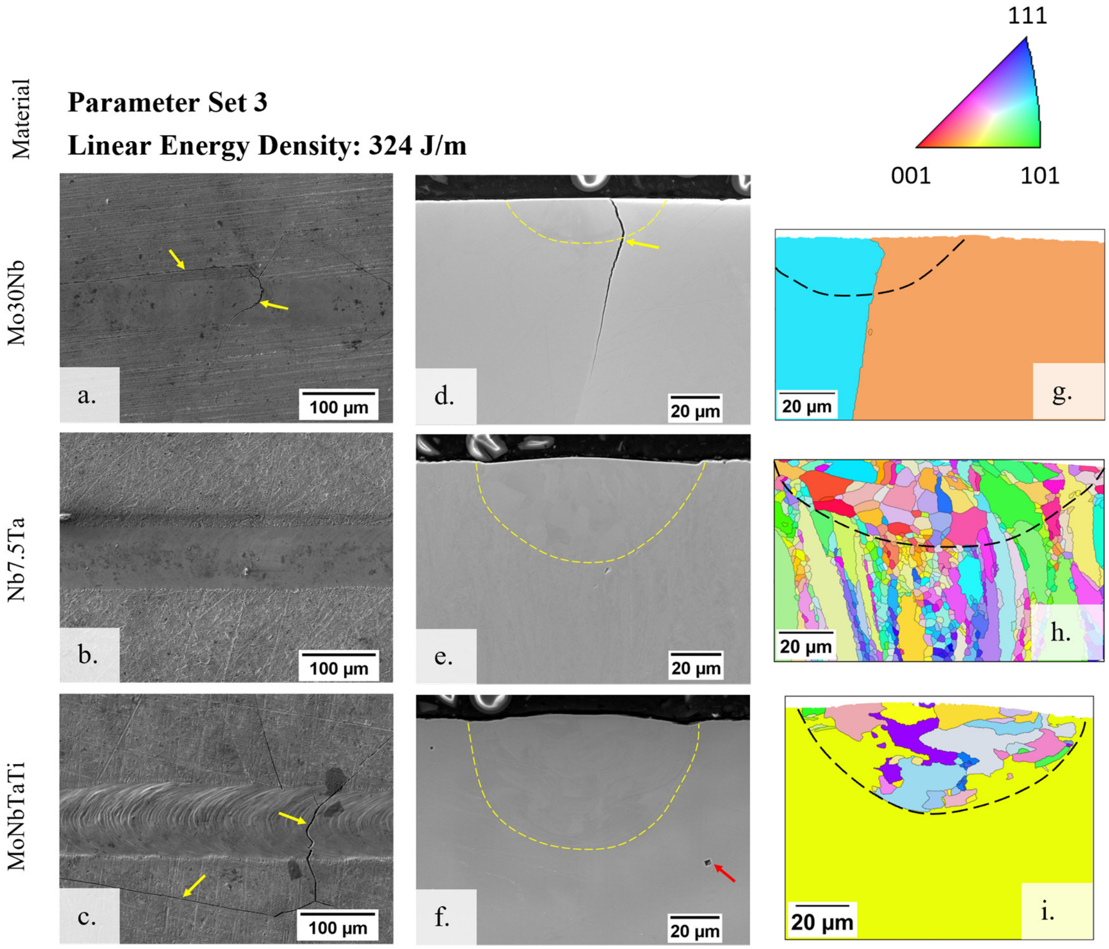

Figure 2.5. Top-down images for melt track 3 on each material are shown in a – c, while the cross sections are shown in d – f and g – i. In these images, yellow arrows indicate cracking, red arrows indicate casting porosity, and blue arrows indicate balling. The IPF maps are shown in g – i. The corresponding alloy is indicated to the left of the images and the IPF key is shown above the IPF maps.

The base material of each alloy was evaluated with EDS to identify the segregation behavior and compare that to the Scheil simulations, as shown in Figure 2.6. Line scans were taken across the dendrites and grain boundaries. The dendrites were unable to be resolved in the Nb7.5Ta due to the rolled structure so only the grain boundaries were targeted. No variation was observed across grains in either of the three alloys, but slight variation was observed across the dendrites that were resolved in the Mo30Nb and MoNbTaTi. Figure 2.6d shows interdendritic regions of the Mo30Nb at about 20 and 75µm and dendritic regions at 45 µm while Figure 2.6f shows an interdendritic region of MoNbTaTi at 10 and 35 µm and a dendritic region at 25 µm. EDS line scans were also completed within each melt track, but no elemental variation was observed.

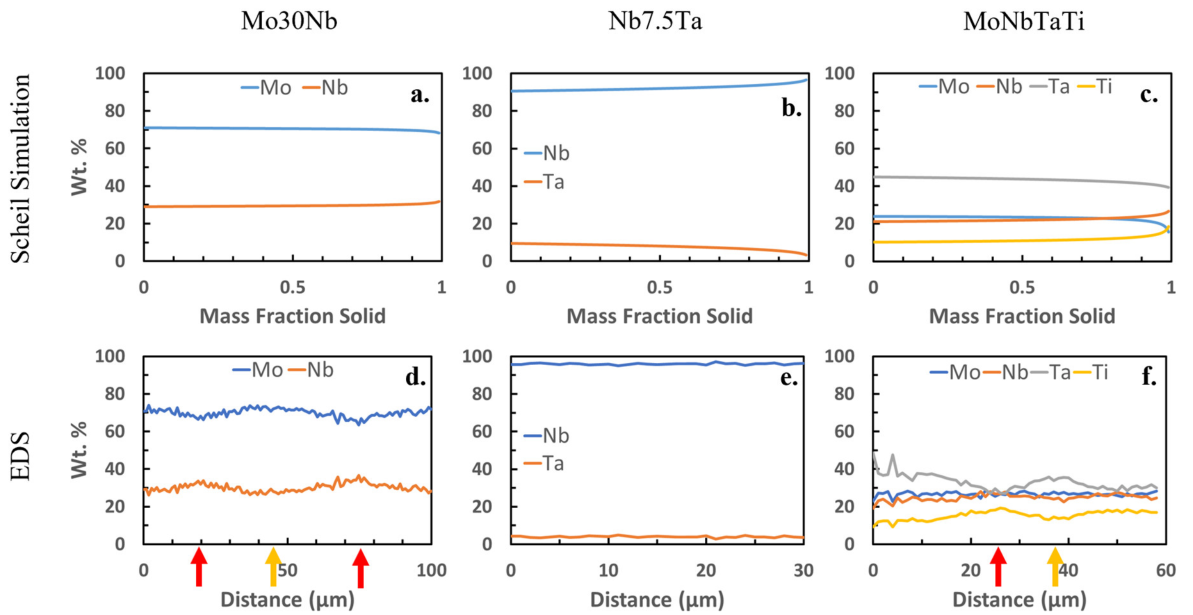

Figure 2.6. Scheil simulations for Mo30Nb, Nb7.5Ta, and MoNbTaTi are shown in a – c. The EDS line scans are also shown for these materials in d – f, respectively. The scans shown in d and f represent dendritic regions while e targeted grain boundaries. Interdendritic regions are indicated with red arrows while dendritic regions are indicated with yellow arrows in d and f.

The width and depth of each melt track were measured in the cross-sectional images in Figure 2.4. This information in combination with the properties modeled for each alloy were used to create material and melt track specific SYSWELD models. The measured and simulated melt track widths and depths are depicted in Table 2.4.

Table 2.4: Measured and simulated melt track widths and depths.

Material	Parameter Set	Linear Energy Density [J/m]]	Measured		Modeled	
			Width [µm]	Depth [µm]	Width [µm]	Depth [µm]
Mo30Nb	1	203	61	19	56	21
	2	1215	169	151	166	138
	3	324	71	17	64	17
	4	238	83	36	80	33
	5	191	62	25	56	22
Nb7.5Ta	1	203	82	28	76	22
	2	1215	314	205	252	159
	3	324	92	38	87	37
	4	238	104	58	94	49
	5	191	90	29	86	27
MoNbTaTi	1	203	73	33	61	28
	2	1215	166	293	166	256
	3	324	94	50	90	47
	4	238	101	69	96	63
	5	191	92	52	86	50

The thermal gradients and cooling rates were predicted with these models and used to create process curves. The modeled thermal gradient was also used to refine the solidification curves, thereby creating not only material-specific maps, but also melt track specific maps. The melt track specific maps for the MoNbTaTi are shown in Figure 2.7. The relative behavior of the process curve for each melt track that is observed for the MoNbTaTi in Figure 2.7 is similar across all three alloys. Note that the thermal gradient and solidification velocity were measured at five points when possible, but several curves have fewer points due to a smaller melt pool tail and mesh size limitations. The bottom point in each curve represents the bottom of the melt pool while the top point represents the top of the melt pool. These points correspond to points 1 and 5, respectively, in Figure 2.3.

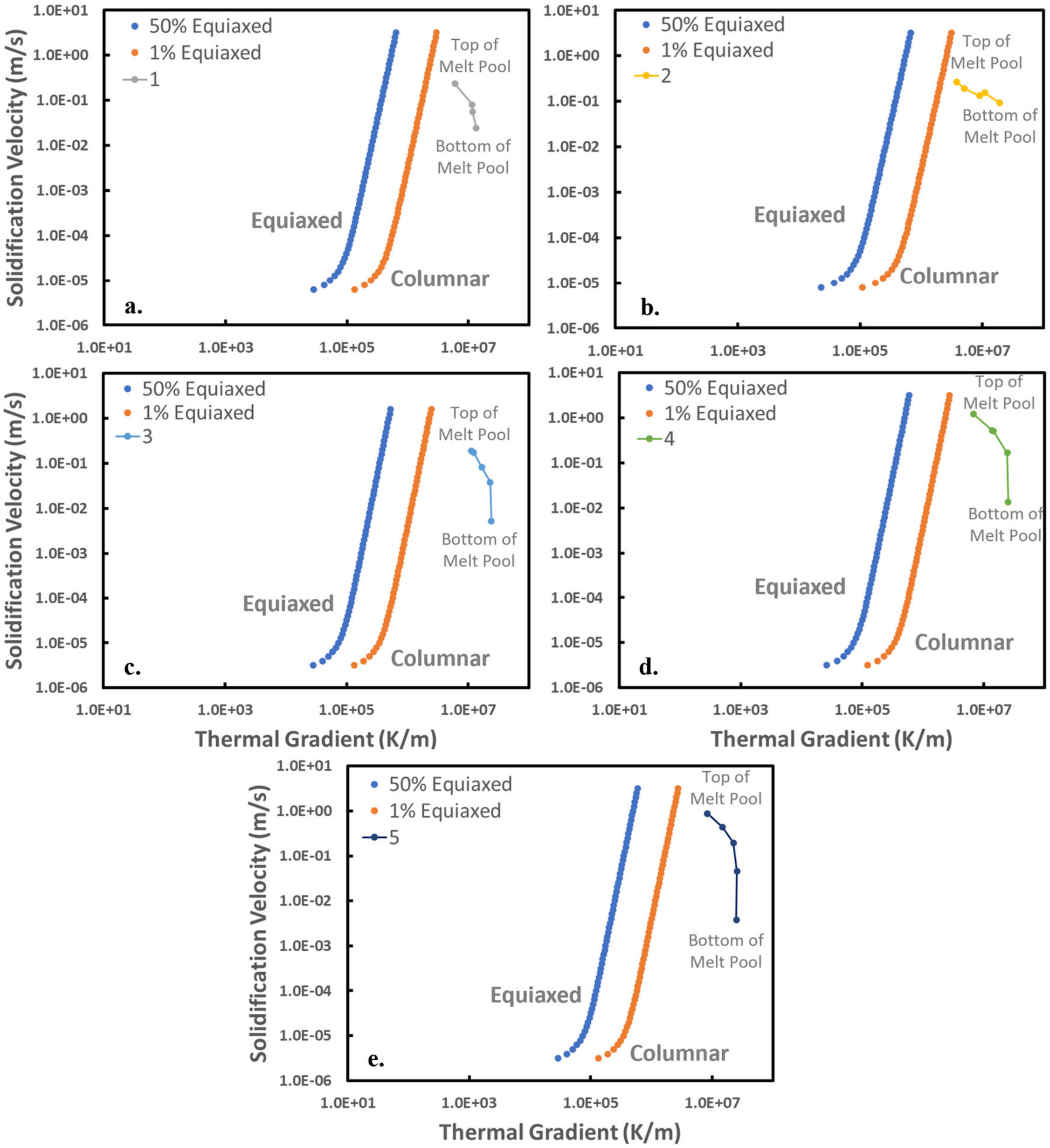

Figure 2.7. Melt track-specific CET solidification maps for each track on MoNbTaTi.

Figure 2.8 compares the maps representing track 3 for all three alloys. The Nb7.5Ta and MoNbTaTi solidification curves were created using alloy-specific nucleation site densities, N_0, on the order of 10^{15} that were approximated from the grain size in the melt pool, G_s, with Equation 2.14. The melt pool grain size of the Mo30Nb was unable to be evaluated due to the epitaxial growth observed, so an experimental value for a Ni-alloy on the order of 10^{12} was used because it has high temperature capabilities similar to those of refractory alloys [17]. The solidification maps that used the estimated alloy-specific nucleation site density were shifted to the right relative to those that used the Ni-alloy; the higher nucleation site density resulted in a higher predicted thermal gradient in the solidification curve. As a result, the Mo30Nb process curves are the furthest away from their solidification curves.

$$\mathrm{G_s} = \frac{1}{\sqrt[3]{\mathrm{N_0}}} \tag{2.14}$$

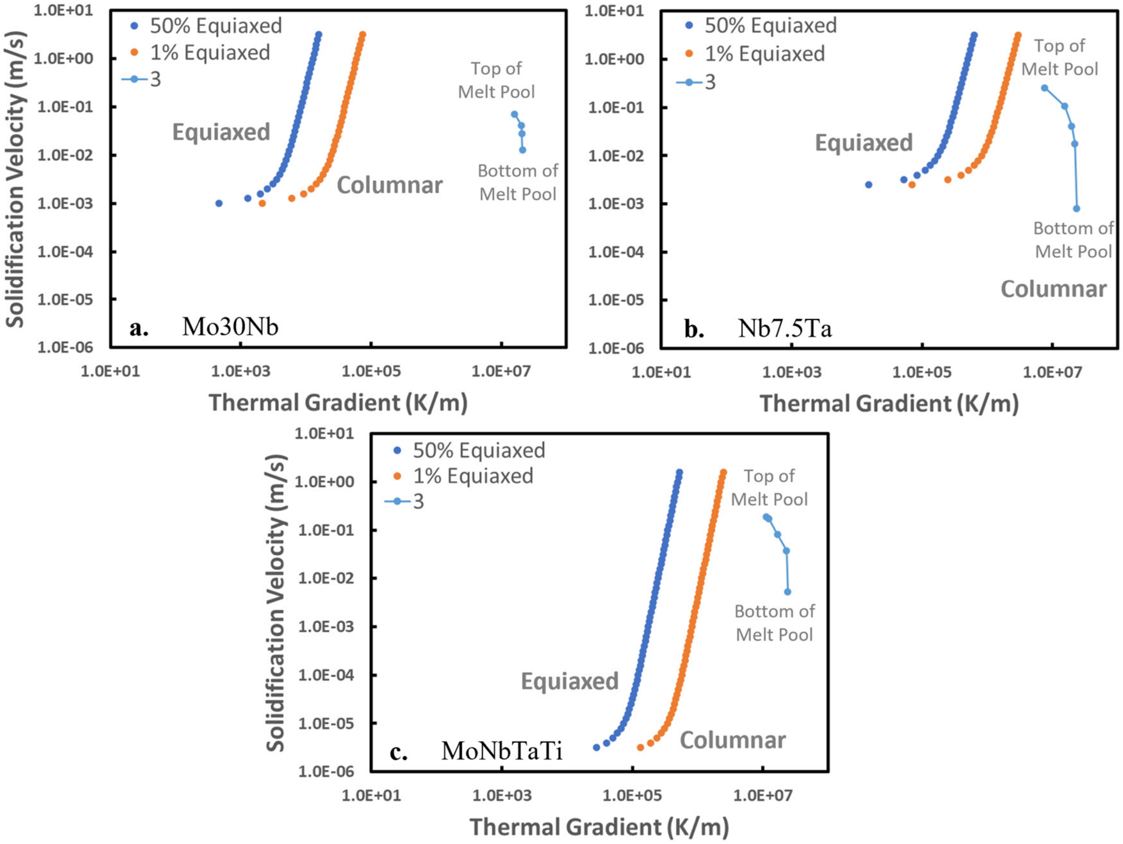

Figure 2.8. CET solidification maps for melt track 3 for Mo30Nb (a), Nb7.5 Ta (b), and MoNbTaTi (c).

2.5 Discussion

The Mo-containing alloys exhibited both solidification cracking within the melt tracks and cracking along the grain boundaries surrounding the melt tracks, as exhibited in Figure 2.5. Solidification cracking, also known as hot cracking, occurs during the final stages of solidification in the melt pool when the mushy region experiences a tensile stress, and the high solid fraction prevents the liquid material from feeding the mushy region to alleviate the stress. This cracking is observed primarily in melt track 2, which exhibited keyholing behavior. The high linear energy density used to create the keyhole can make the melt track more susceptible to solidification cracking [18]. The grain boundary cracking observed is indicative of the high crack susceptibility of Mo because no preheat was applied when creating the single-track melts. The solid solution strengthening model presented by F. G. Coury et al. was applied to these three alloys to estimate and compare their room temperature strengths [19, 20]. The model includes athermal and thermal components. The thermal component calculation requires experimental data, which is only available for the MoNbTaTi, but the athermal component can be calculated with just the properties of the constituent elements. As a result, only the athermal component of yield strength was calculated for each alloy, which can be used as an indicator of the relative strengths of the alloys. The predicted athermal contributions to yield strength are 562, 51, and 540 MPa for the Mo30Nb, the Nb7.5Ta, and the MoNbTaTi, respectively. The high predicted values for the Mo30Nb and the MoNbTaTi indicate that they are more susceptible to cracking and therefore cracked during the laser melt track processing. Applying a preheat above the ductile-brittle transition temperature would mitigate the risk of grain boundary cracking. This has been proven to successfully eliminate cracking during the joining of various Mo-alloys [21, 22].

Impurities such as oxygen and nitrogen also contributed to the grain boundary cracking in the Mo-containing alloys. Similar cracking was observed in a separate study evaluating a LPBF build of pure (elemental) molybdenum. It was found that the grain boundary embrittlement and cracking was caused by segregated oxygen; molybdenum oxides were discovered at the intergranular fracture surfaces [23]. The oxygen segregation and therefore the grain boundary cracking can be mitigated by increasing the carbon content. This method has been found to successfully reduce cracking in welded Mo-alloys [24]. Embrittlement is also caused by an increased nitrogen content. A similar Mo-containing RHEA, MoNbTaWV, thin film was doped with nitrogen to achieve an increase in hardness, but this was accompanied by embrittlement due to the formation of nitrides [25]. The Mo30Nb and MoNbTaTi reported higher levels of nitrogen and oxygen, respectively.

The segregation behavior observed in the Mo30Nb and MoNbTaTi both agreed with the Scheil simulations, which indicates that the CALPHAD databases are capable of accurately predicting partitioning in these alloys. This aligns with behavior observed in the RHEA systems NbTaV- (Ti, W), where it was found that the dendritic segregation behavior in as-cast material aligned with the simulated segregation behavior [26]. The segregation within the melt pools was unable to be observed for all three alloys in this investigation because the length scale in the melt pool is finer than that in the base material; the energy resolution of the EDS detector in the TESCAN is not small enough to distinguish the differences in energies on the finest scale within the melt pool. Similar analyses have been conducted on the MoNbTaW, where dendritic segregation in an as-cast sample was able to be measured while that in an LPBF-processed sample was similarly too fine to be resolved with an SEM. In that LPBF sample, the dendrite length scale was an order of magnitude smaller than in the comparable as-cast material [27, 28].

Melt tracks 4 and 5 both exhibited balling in the Nb7.5Ta and MoNbTaTi while only melt track 4 exhibited the effect for the Mo30Nb. This balling effect is observable as instability or breaks in the melt track are caused by non-optimal laser parameters and can cause defects in a full build [29]. The balling is the result of capillary instability in the melt pool that occurs when there is a high ratio between its length and width. This often occurs at high laser scan speeds. The melt pool breaks to lower the surface energy of this condition. The point at which the melt pool breaks is defined by the Rayleigh instability, which dictates that the length of the cylindrical melt pool cannot exceed its circumference. When this criterion is surpassed, balling occurs [30]. Balling has been observed in various alloys, including Ni-based superalloys and stainless steels, produced via LPBF. In these studies, balling has been attributed to the low linear energy density that often accompanies a high laser scan speed [31, 32]. Melt tracks 4 and 5 were both created with the highest speed used. The presence of balling in these melt tracks indicates that the slower speeds used for melt tracks 1-3 are more suitable for these alloys.

Similar trends in the melt pool shapes and sizes for each track are observed across the alloys in the cross sections. In a study conducted on an LPBF-processed Al-alloy, it was determined that the laser parameters had the greatest effect on the shape and size of the melt pool; laser power had the greatest effect on melt pool depth while laser scan speed had the greatest effect on melt pool width [33]. However, differences are observed when the grain morphology was evaluated with EBSD. In a study examining the behavior of various Ti-alloys under similar laser conditions, it was found that the alloy composition and its corresponding undercooling had the greatest influence over the melt pool grain morphology [34]. The Nb7.5Ta and MoNbTaTi both exhibit nucleation of new grains within the melt pool while the Mo30Nb exhibits only epitaxial growth. In a study evaluating the grain morphology evolution in a Ni-based superalloy under laser AM conditions, the new grain nucleation and CET behavior observed was found to be dependent on the total undercooling of the system [35]. The total undercooling for Mo30Nb is less than for Nb7.5Ta and MoNbTaTi, as shown in Figure 2.9, and can be attributed for this difference in behavior; the low undercooling did not allow nucleation sites to grow in the liquid ahead of the solid-liquid interface during solidification.

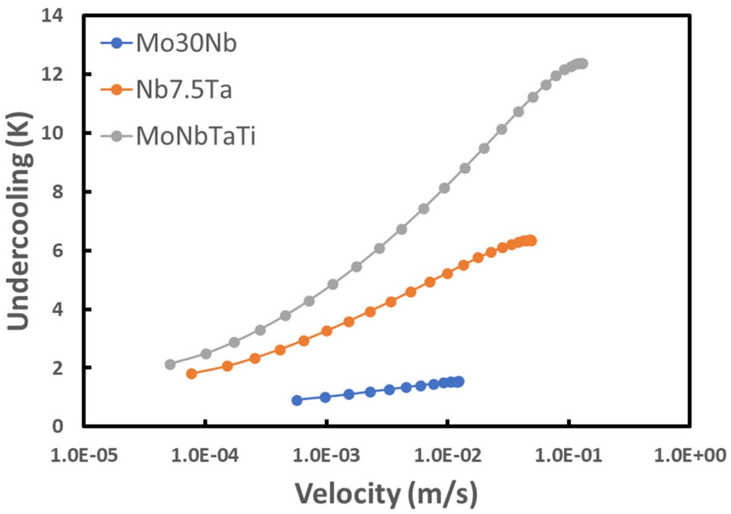

Figure 2.9. A comparison of the total undercooling of each alloy.

The total undercooling of the system can also be used to explain the CET behavior. The total undercooling is expected to be low at the bottom of the melt pool, hence there is very little driving force for heterogeneous nucleation and grains are expected to grow epitaxially. At the top of the melt pool, the undercooling is increased so heterogeneous nucleation is expected. This results in the equiaxed grains being concentrated near the centerline of the melt pool in the Nb7.5Ta and MoNbTaTi melt pools which all displayed new grain nucleation [35].

Solidification maps were created for each alloy to predict the CET behavior and final microstructure of each melt track. The G-V process curves are observed to be further from the solidification curve for the Mo30Nb than for the Nb7.5Ta and MoNbTaTi when comparing the CET curves presented in Figure 2.8. This difference can be indicative of the difference in total undercooling displayed in Figure 2.9. The maps predict that every alloy and condition combination will form a columnar structure throughout the melt pool, which is not consistent with the experimental results. A summary of the experimental and predicted results is depicted in Table 2.5. The same solidification modeling employed in this study was previously evaluated for both Ni and Al alloys. This model assumes that every possible nucleation site becomes a grain, which is not representative of typical experimentation. Despite this, the models for both the Ni and Al-alloys corresponded to the experimental results [13]. This suggests that the modeling procedure used to create the maps depicted in Figures 2.7 and 2.8 can produce accurate results. Therefore, the input parameters being used for the refractory alloy modeling were examined for their effect on the inaccuracies observed in the model.

Table 2.5: Summary of the experimental and predicted grain morphology.

Material	Parameter Set	Linear Energy Density [J/m]	Experimental	Predicted
Mo30Nb	1	203	Only epitaxial growth observed	Columnar
	2	1215	Equiaxed	Columnar
	3	324	Only epitaxial growth observed	Columnar
	4	238	Only epitaxial growth observed	Columnar
	5	191	Only epitaxial growth observed	Columnar
Nb7.5Ta	1	203	Equiaxed	Columnar
	2	1215	Equiaxed	Columnar
	3	324	Equiaxed	Columnar
	4	238	Equiaxed	Columnar
	5	191	Equiaxed	Columnar
MoNbTaTi	1	203	Equiaxed	Columnar
	2	1215	Equiaxed	Columnar
	3	324	Equiaxed	Columnar
	4	238	Equiaxed	Columnar
	5	191	Equiaxed	Columnar

The nucleation site density, which is used to create the CET curves and affects its horizontal position, is an approximated value. Material-specific nucleation site densities were approximated for the Nb7.5Ta and MoNbTaTi with the measured melt pool grain size. These higher nucleation site densities were found to shift the curves to the right, thereby bringing them closer to the process curves. However, this shift did not resolve the inaccuracies observed when using the nucleation site density of a Ni-based superalloy. It was therefore determined that the approximated nucleation site density was not the primary source of error in the CET models.

An approximate value was also used for the Gibbs-Thomson coefficient, which is used in the KGT model. An experimental value for a Ni-alloy was used for all three alloys in this study. To determine the effect the Gibbs-Thomson coefficient, Γ, has on the solidification map calculations, its minimum and maximum values for each alloy were calculated with Equation 2.15 [36]. A similar sensitivity analysis was conducted for the Gibbs-Thomson coefficient in a Ni-alloy, the outcome of which indicated that the Gibbs-Thomson coefficient did not have a significant effect on the final solidification model [10].

$$\Gamma = \frac{T_m * \gamma_{sl} * V_m}{L_m} \tag{2.15}$$

The latent heat of fusion, L_m, for pure Mo was used for the Mo30Nb while pure Nb was used for the Nb7.5Ta and MoNbTaTi. The melting temperature, T_m, and molar volume, V_m, were calculated for each alloy while the solid-liquid interfacial energy, γ_{sl},was varied between its minimum and maximum. These parameters are shown in Table 2.6.

Table 2.6: Gibbs-Thomson coefficient minimum and maximum estimations with input parameters.

Material	**T_m [K]**	**V_m [m^3/mol]**	**L_m [J/mol] [37]**	**γ_{sl} [J/m^2] [36]**	**Γ [K-m]**
Mo30Nb	2856	9.8E-06	35600	0.03	2.35E-08
				0.3	2.35E-07
Nb7.5Ta	2769	1.1E-05	29300	0.03	3.08E-08
				0.3	3.08E-07
MoNbTaTi	2875	1.0E-05	29300	0.03	3.04E-08
				0.3	3.04E-07

The Ni-alloy Gibbs-Thomson coefficient used for the solidification modeling falls within the range of the minimum and maximum calculated Gibbs-Thomson coefficient. The effect that this change in Gibbs-Thomson coefficient has on the solidification model can be quantified by completing a primary dendrite arm spacing (PDAS) calculation and comparing that to the previously measured values that are reflected for melt track 3 in Table 2.7. This method was previously employed to evaluate the effectiveness of solidification models for both Ni and Al-alloys. In that analysis, the average measured and calculated values were found to be 0.4 and 0.5 µm, respectively. The measured and calculated PDAS values are expected to differ by less than an order of magnitude in an accurate model [13].

The PDAS was measured according to Figure 2.10, which shows example of an area used for the PDAS measurement. Several areas where approximately ten dendrites could be resolved were measured and averaged to generate each value.

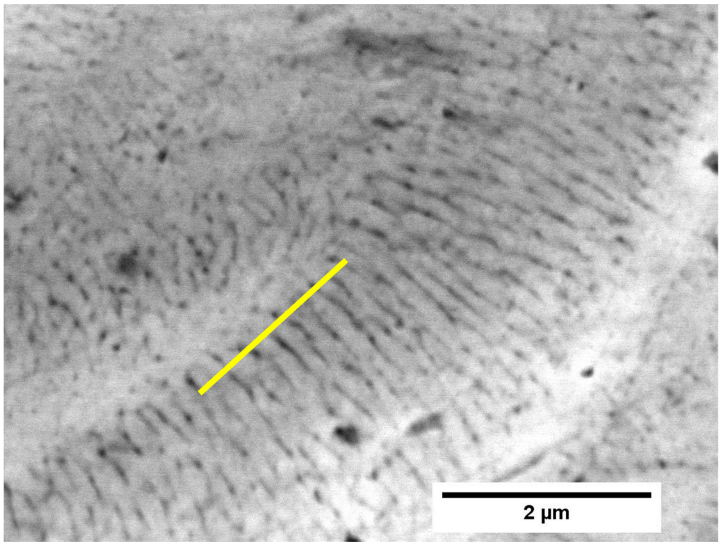

Figure 2.10. Backscatter image of track 1 in MoNbTaTi showing primary dendrites near the bottom of the melt pool. The yellow line indicates an example measurement area.

The PDAS, λ, is calculated with Equation 2.16. In Equation 2.16, R is the tip radius, $\Delta T_0'$ is the non-equilibrium freezing range and G is the modeled thermal gradient. The tip radius is a function of solidification velocity V, as shown in Equation 2.17. This relationship is established as part of the KGT model by plotting tip radius as a function of solidification velocity. In Equation 2.17, α and $\beta$are constants taken from a power law fit that is created to model the tip radius and solidification velocity plot. The non-equilibrium freezing range is calculated with Equation 2.18, in which T_{tip} is the liquidus temperature and T_{base} is the non-equilibrium solidus temperature. The material and melt track specific modeled thermal gradients were used for each PDAS calculation. This allowed PDAS to be predicted for each melt track in each material [37].

$$\lambda = \sqrt{\frac{3R\Delta T_o'}{G}} \tag{2.16}$$

$$R = \alpha V^{\beta} \tag{2.17}$$

$$\Delta T_o' = T_{tip} - T_{base} \tag{2.18}$$

The PDAS calculated at the bottom of the melt pool for these processing conditions with the Ni-alloy Gibbs-Thomson coefficient were within approximately an order of magnitude of the measured values for all three alloys. The Mo30Nb measured and calculated values are closer than those of the Nb7.5Ta and the MoNbTaTi, but the reason for this difference in behavior could not be accounted for reliably with the information available. Although the calculated minimum and maximum Gibbs-Thomson coefficients for each material ranged by an order of magnitude, the resultant PDAS calculations for the bottom of the melt pool varied only slightly and were still within approximately an order of magnitude, as shown in Table 2.7. The PDAS calculated with the Ni-alloy Gibbs-Thomson coefficient fell within the range of calculated PDAS for the minimum and maximum Gibbs-Thomson coefficients for each alloy. Therefore, it was determined that the approximated Gibbs-Thomson coefficient was not the primary source of error in the solidification models.

The accuracy of the solidification model was further evaluated investigating the effect each variable in Equation 2.16 has on the calculated PDAS.

Table 2.7: PDAS calculated with the Ni-alloy and approximated Gibbs-Thomson coefficients and the measured PDAS for melt track 3.

Material	**Measured PDAS [m]**	**PDAS Calculated with Ni-alloy Γ [m]**	**PDAS Calculated with Minimum Γ [m]**	**PDAS Calculated with Maximum Γ [m]**	**PDAS Calculated with Rosenthal model [m]**
Mo30Nb	2.9E-07	9.9E-07	4.8E-07	1.1E-06	2.9E-07
Nb7.5Ta	2.1E-07	1.8E-06	6.3E-07	2.1E-06	3.5E-07
MoNbTaTi	4.7E-07	2.9E-06	1.4E-06	4.0E-06	1.2E-06

The tip radius, R, is a function of the modeled solidification velocity and the KGT model input parameters. It has already been determined that the approximated Gibbs-Thomson coefficient does not have a significant impact on the results of the KGT model and predicted tip radius. However, the modeled liquidus slopes and partitioning coefficients used in the KGT model also affect the predicted tip radius. The relationship between tip radius and PDAS has been established for a Ni-based superalloy; tip radius and PDAS are directly related [38]. Due to the experimental data currently available for refractory alloys, the accuracy of modeled liquidus slopes and partitioning coefficients is unable to be assessed. Increasing the liquidus slopes and moving the partitioning coefficients further from one for each solute element both decrease the predicted PDAS. This indicates that the current refractory databases may not be accurately predicting the liquidus slopes and partitioning coefficients for these alloy systems. Higher predicted solidification velocities, which are dependent on the thermal gradient modeling, would also result in smaller predicted PDAS.

$\Delta T_0'$ is calculated by subtracting the non-equilibrium solidus, which is modeled using Scheil simulations, from the liquidus temperature. It is expected to decrease as the total undercooling of the system decreases. A wrought Al study found this trend to be true [39]. This trend is observed as the Mo30Nb displays the lowest non-equilibrium freezing range while MoNbTaTi displays the highest, which corresponds to the undercooling represented in Figure 2.9. The calculated values for Mo30Nb, Nb7.5Ta, and MoNbTaTi are 4, 16, and 168 °C, respectively. The non-equilibrium freezing range has been modeled in other studies for Ni-based superalloys and found to be in the range of 175 °C, indicating that the higher calculated value for MoNbTaTi may be reasonable [40]. The higher calculated value for MoNbTaTi likely contributed to the larger than expected calculated PDAS. This indicates that the appropriate trends can be predicted, but the accuracy of the values cannot be substantiated.

SYSWELD uses a normally distributed heat source to model a representative the thermal gradient [41]. The Rosenthal model assumes a point heat source, and higher thermal gradients are predicted for each of the melt tracks [42]. The distributed heat source is generally considered to produce more accurate results than the point heat source, which was established in a study conducted on laser engineered net shaping (LENS) of Al-alloys [43]. When used to calculate PDAS, the higher thermal gradients from the Rosenthal model predict smaller PDAS values that are closer to the measured values. The calculated Mo30Nb PDAS is equivalent to the measured PDAS. However, the predicted values for Nb7.5Ta and MoNbTaTi remain inaccurate, though they are closer to the measured value. The temperature gradients calculated from the Rosenthal model can be considered the highest within reason, so other factors must contribute to the discrepancy between microstructure predictions and experimental measurements.

While the position of the process curves relative to the solidification curves was determined to be inconsistent with experimental results, the shape of the curves and general trends observed are consistent with the processing conditions. The top of the melt pool is expected to have a solidification velocity close to the laser scan speed while the bottom of the melt pool is expected to have a solidification velocity approximately two orders of magnitude lower. This is generally observed across all the melt tracks, as shown for MoNbTaTi in Figure 2.7. Melt tracks 4 and 5 exhibit the highest modeled solidification velocity at the top of the melt pool, which corresponds to the laser parameters used in the experiment. This is expected because higher laser speeds cause higher cooling rates, which correlates to a higher solidification velocity [44]. The shape and location of the G-V path for melt track 2 is inconsistent with the others. This can be attributed to the keyholing behavior that it exhibited; because only conduction heat transfer was considered, it is not able to fully characterize this behavior. For instance, the modeled melt pool dimensions for the Nb7.5Ta melt track 2 were approximately 20% lower than what was measured, which caused the predicted process curves to shift left relative to the others. Accounting for convection in addition to conduction would more accurately simulate the temperature fields in melt track 2. The mesh size used by SYSWELD may also contribute to some of the inaccuracies observed; the minimum achievable mesh size is not robust enough to fully characterize a laser-based system. Similar limitations were observed in SYSWELD in a Ti-alloy study [45].

While the relative trends of the process curves for each melt track within a single alloy is consistent with what is displayed for MoNbTaTi in Figure 2.7, the shape of the process curves for each alloy differs slightly. This is observable in Figure 2.8, where the Mo30Nb curve is seen to be the shortest, the Nb7.5Ta is seen to have the steepest curve, and the MoNbTaTi is seen to be the most linear. The shape of the processing curves varies between alloys due to the difference in the modeled thermomechanical properties for each and the effect they have on thermal gradient predictions. The density, specific heat, and thermal conductivity modeled as a function of temperature for each alloy are shown compared to the modeled data for pure Nb in Figure 2.11. The plots for pure Nb were also modeled in Thermo-Calc and is used as a point of comparison because this system is well characterized in CALPHAD databases. It’s thermophysical properties have been measured and documented in both the solid and liquid phases [46, 47].

The predicted shapes of the density curves for the three alloys are very similar to that predicted for pure Nb. All three alloys predict a higher density than that of pure Nb because Nb has a lower density than the Mo and Ta that are present in the refractory alloys. The predicted shapes of the specific heat curves for the three alloys are similar, but Mo30Nb exhibits a greater change at its liquidus temperature than pure Nb and the other two alloys. The predicted shapes of the thermal conductivity curves for Nb.7.5Ta and MoNbTaTi are like what is predicted for pure Nb. The predicted conductivity values are lower for the alloys than for the pure material, which is expected [48]. The Mo30Nb curve is the only plot that exhibits a negative slope before reaching the liquidus temperature. The validity of the predicted thermophysical properties for the refractory alloys cannot be accurately assessed at this time due to the lack of available data. However, by comparing them to a similar known material, conclusions can be drawn about the accuracy of the predicted trends; based on the plots observed in Figure 2.11, it can be concluded that the Nb7.5Ta and MoNbTaTi predictions exhibit more accurate trends than the Mo30Nb prediction. However, further characterization of the thermal conductivity and the other thermophysical properties should be completed for these alloy systems to allow for more accurate thermal gradient predictions.

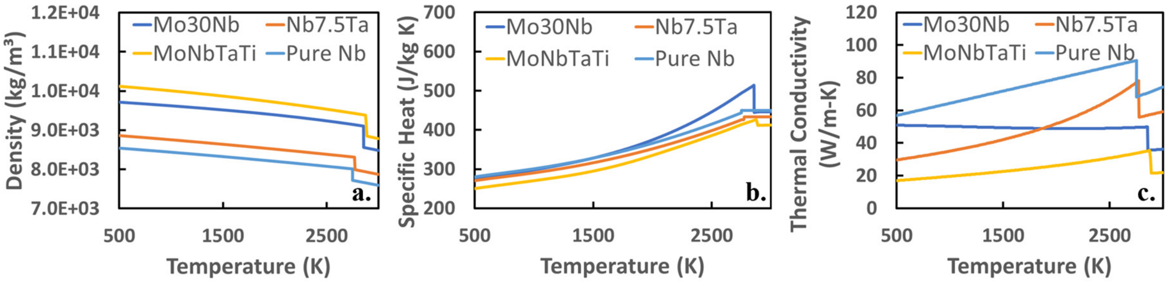

Figure 2.11. CALPHAD property predictions of density (a.), specific heat (b.), and thermal conductivity (c.) of each alloy of interest as well as pure Nb.

2.6 Conclusions

Ultimately, this investigation succeeded in showing that the microstructure of refractory alloys can be manipulated by changing the laser parameters. The shape and size of each melt pool as it related to the processing parameters was similar across all three alloys, though the grain morphology was not consistent. The Mo-containing alloys were found to exhibit cracking during processing due to their higher strength. This information can be used in guiding future laser parameter selection. For instance, it can be concluded that melt track 2 (linear energy density: 1215 J/m) produced deleterious keyholing while melt tracks 4 and 5 (linear energy density: 238, 191 J/m) produced balling, making all three parameter sets unideal for AM of refractory alloys. Parameter set 3 (linear energy density: 324 J/m) exhibited the most ideal behavior across all three alloys. It can also be concluded that the Mo-containing alloys require a preheat above the ductile-brittle transition temperature to mitigate cracking.

The material databases used were shown to be capable of predicting general trends; the Schiel simulations aligned with EDS measurements, the non-equilibrium freezing range correlates with the relative total undercooling of each alloy, and the trends of the process curves aligned with the laser parameters used experimentally. However, the material databases ultimately proved insufficient when used to model the properties of these refractory alloy, as demonstrated by the microstructure predictions not corresponding to the experimental results. While the actual modeled values are unable to be validated with the currently available data for these alloys, the likely changes in the values needed to create an accurate model were able to be predicted.

Therefore, the material property databases for refractory alloys, specifically as they relate to liquidus slope, partitioning coefficient, solid-liquid interfacial energies, and thermophysical properties, needs to be expanded to enable the development and calibration of accurate solidification models for these alloy systems.

2.7 Acknowledgements

Thank you to ATI Specialty Alloys and Components for providing material and material data in support of this project. This work was funded by the Department of Energy's Kansas City National Security Campus (KSCNC) which is operated and managed by Honeywell Federal Manufacturing Technologies, LLC under contract number DE-NA0002839. Thank you also to Sandia National Laboratories for their support. Sandia National Laboratories is a multimission laboratory managed and operated by National Technology and Engineering Solutions of Sandia LLC, a wholly owned subsidiary of Honeywell International Inc. for the U.S. Department of Energy's National Nuclear Security Administration under contract DE-NA0003525. This paper describes objective technical results and analysis. Any subjective views or opinions that might be expressed in the paper do not necessarily represent the views of the U.S. Department of Energy or the United States Government. Lab facilities at KCNSC, ATI, and Colorado School of Mines were used to support this work. This research used resources of the TESCAN S8252G RAMAN-SEM/FIB at the Colorado School of Mines which was acquired through the support of the National Science Foundation (DMR-1828454). I appreciate the contributions of Alec Saville, Chris Jasien, Nate Peterson, and Zane Fisher.

2.8 References

[1] N. R. Philips, M. Carl, and N. J. Cunningham, "New opportunities in refractory alloys," *Metallurgical and Materials Transactions*, vol. 51, no. 7, pp. 3299–3310, 2020.

[2] Y.-Zheng Yang, J.-ling Yang, and D.-Ning Fang, "Research progress on thermal protection materials and structures of hypersonic vehicles," *Applied Mathematics and Mechanics*, vol. 29, no. 1, pp. 51–60, 2008.

[3] B. S. Murty, J. W. Yeh, and S. Ranganathan, "Chapter 2 - High-Entropy Alloys: Basic Concepts," in *High entropy alloys*, Butterworth-Heinemann, 2014.

[4] Y. F. Ye, Q. Wang, J. Lu, C. T. Liu, and Y. Yang, "High-entropy alloy: Challenges and prospects," *Materials Today*, vol. 19, no. 6, pp. 349–362, 2016.

[5] Y. Zhang and Q. Xing, "High entropy alloys: Manufacturing Routes," *Encyclopedia of Materials: Metals and Alloys*, pp. 327–338, 2022.

[6] J. M. Torralba and M. Campos, "High entropy alloys manufactured by Additive Manufacturing," *Metals*, vol. 10, no. 5, p. 639, 2020.

[7] Thermo-Calc Software TCHEA version 5.1, January 2022.

[8] S. Bontha, N. W. Klingbeil, P. A. Kobryn, and H. L. Fraser, “Thermal process maps for predicting solidification microstructure in laser fabrication of thin-wall structures,” *Journal of Materials Processing Technology*, vol. 178, no. 1-3, pp. 135–142, 2006.

[9] W. Kurz, B. Giovanola, and R. Trivedi, “Theory of microstructural development during Rapid Solidification,” *Acta Metallurgica*, vol. 34, no. 5, pp. 823–830, 1986.

[10] M. Haines, A. Plotkowski, C. L. Frederick, E. J. Schwalbach, and S. S. Babu, “A sensitivity analysis of the columnar-to-equiaxed transition for ni-based superalloys in electron beam additive manufacturing,” *Computational Materials Science*, vol. 155, pp. 340–349, 2018.

[11] M. R. Rolchigo and R. LeSar, “Modeling of binary alloy solidification under conditions representative of Additive Manufacturing,” *Computational Materials Science*, vol. 150, pp. 535–545, 2018.

[12] R. Prichard, M. Gibson, C. Joseph, and W. Strasser, “A review of fluid flow in and around the brain, modeling, and abnormalities,” *Multiscale Biomechanical Modeling of the Brain*, pp. 209–238, 2022.

[13] P. Mohammadpour and A. B. Phillion, “Solidification microstructure selection maps for laser powder bed fusion of multicomponent alloys,” *IOP Conference Series: Materials Science and Engineering*, vol. 861, no. 1, p. 012005, 2020.

[14] M. Gäumann, C. Bezençon, P. Canalis, and W. Kurz, “Single-crystal laser deposition of superalloys: Processing–microstructure maps,” *Acta Materialia*, vol. 49, no. 6, pp. 1051–1062, 2001.

[15] C. Beckermann, “Macrosegregation,” *Encyclopedia of Materials: Science and Technology*, pp. 4733–4738, 2001.

[16] T. S. Srivatsan and T. S. Sudarshan, “The influence of phosphorus on shrinkage porosity in cast irons,” *Materials Letters*, vol. 41, no. 4, pp. 186–191, 1999.

[17] M. Steinzig, “Stochastic characterization of cast metal microstructure,” thesis, United States. Dept. of Energy, Washington, D.C, 1999.

[18] B. Mondal, M. Gao, T. A. Palmer, and T. DebRoy, “Solidification cracking of a nickel alloy during high-power keyhole mode laser welding,” *Journal of Materials Processing Technology*, vol. 305, p. 117576, 2022.

[19] F. G. Coury, M. Kaufman, and A. J. Clarke, “Solid-solution strengthening in refractory high entropy alloys,” *Acta Materialia*, vol. 175, pp. 66–81, 2019.

[20] B. C. Peters and A. A. Hendrickson, “Solid solution strengthening in Nb-Ta and nb-mo alloy single crystals,” *Metallurgical Transactions*, vol. 1, no. 8, pp. 2271–2280, 1970.

[21] D. Wang, C. Yu, J. Ma, W. Liu, and Z. Shen, “Densification and crack suppression in selective laser melting of pure molybdenum,” *Materials & Design*, vol. 129, pp. 44–52, 2017.

[22] B. Tabernig and N. Reheis, “Joining of molybdenum and its Application,” *International Journal of Refractory Metals and Hard Materials*, vol. 28, no. 6, pp. 728–733, 2010.

[23] J. Braun, L. Kaserer, J. Stajkovic, K.-H. Leitz, B. Tabernig, P. Singer, P. Leibenguth, C. Gspan, H. Kestler, and G. Leichtfried, “Molybdenum and tungsten manufactured by Selective Laser Melting: Analysis of defect structure and Solidification Mechanisms,” *International Journal of Refractory Metals and Hard Materials*, vol. 84, p. 104999, 2019.

[24] J. Wadsworth, T. G. Nieh, and J. J. Stephens, “Recent advances in aerospace refractory metal alloys,” *International Materials Reviews*, vol. 33, no. 1, pp. 131–150, 1988.

[25] A. Xia, R. Dedoncker, O. Glushko, M. J. Cordill, D. Depla, and R. Franz, “Influence of the nitrogen content on the structure and properties of MoNbTaVW high entropy alloy thin films,” *Journal of Alloys and Compounds*, vol. 850, p. 156740, 2021.

[26] H. W. Yao, J. W. Qiao, M. C. Gao, J. A. Hawk, S. G. Ma, H. F. Zhou, and Y. Zhang, “NbTaV-(Ti,W) refractory high-entropy alloys: Experiments and modeling,” *Materials Science and Engineering*, vol. 674, pp. 203–211, 2016.

[27] O. N. Senkov, G. B. Wilks, D. B. Miracle, C. P. Chuang, and P. K. Liaw, “Refractory high-entropy alloys,” *Intermetallics*, vol. 18, no. 9, pp. 1758–1765, 2010.

[28] H. Zhang, Y. Zhao, S. Huang, S. Zhu, F. Wang, and D. Li, “Manufacturing and analysis of high-performance refractory high-entropy alloy via selective laser melting (SLM),” *Materials*, vol. 12, no. 5, p. 720, 2019.

[29] M. Król and T. Tański, “Surface Quality Research for selective laser melting of ti-6al-4v alloy,” *Archives of Metallurgy and Materials*, vol. 61, no. 3, pp. 1291–1296, 2016.

[30] A. V. Gusarov, I. Yadroitsev, P. Bertrand, and I. Smurov, “Heat transfer modelling and stability analysis of selective laser melting,” *Applied Surface Science*, vol. 254, no. 4, pp. 975–979, 2007.

[31] Q. Guo, C. Zhao, M. Qu, L. Xiong, S. M. Hojjatzadeh, L. I. Escano, N. D. Parab, K. Fezzaa, T. Sun, and L. Chen, “In-situ full-field mapping of melt flow dynamics in laser metal additive manufacturing,” *Additive Manufacturing*, vol. 31, p. 100939, 2020.

[32] R. Li, J. Liu, Y. Shi, L. Wang, and W. Jiang, “Balling behavior of stainless steel and nickel powder during selective laser melting process,” *The International Journal of Advanced Manufacturing Technology*, vol. 59, no. 9-12, pp. 1025–1035, 2011.

[33] Q. Guo, C. Zhao, M. Qu, L. Xiong, L. I. Escano, S. M. Hojjatzadeh, N. D. Parab, K. Fezzaa, W. Everhart, T. Sun, and L. Chen, “In-situ characterization and quantification of melt pool variation

under constant input energy density in laser powder bed fusion additive manufacturing process," *Additive Manufacturing*, vol. 28, pp. 600–609, 2019.

[34] Y.-Y. Zhu, H.-B. Tang, Z. Li, C. Xu, and B. He, "Solidification behavior and grain morphology of laser additive manufacturing titanium alloys," *Journal of Alloys and Compounds*, vol. 777, pp. 712–716, 2019.

[35] P. Liu, Z. Wang, Y. Xiao, M. F. Horstemeyer, X. Cui, and L. Chen, "Insight into the mechanisms of columnar to equiaxed grain transition during metallic additive manufacturing," *Additive Manufacturing*, vol. 26, pp. 22–29, 2019.

[36] J. A. Dantzig and M. Rappaz, *Solidification*, 2nd Edition. Lausanne, Suisse: EPFL Press, 2016.

[37] "Thermochemical Data," Smithells Metals Reference Book, 2004.

[38] W. Xiao, S. Li, C. Wang, Y. Shi, J. Mazumder, H. Xing, and L. Song, "Multi-scale simulation of dendrite growth for direct energy deposition of nickel-based superalloys," *Materials & Design*, vol. 164, p. 107553, 2019.

[39] S. Lin, C. Aliravci, and M. O. Pekguleryuz, "Hot-tear susceptibility of aluminum wrought alloys and the effect of grain refining," *Metallurgical and Materials Transactions*, vol. 38, no. 5, pp. 1056–1068, 2007.

[40] R. Thavamani, V. Balusamy, J. Nampoothiri, R. Subramanian, and K. R. Ravi, "Mitigation of hot cracking in Inconel 718 superalloy by ultrasonic vibration during gas tungsten arc welding," *Journal of Alloys and Compounds*, vol. 740, pp. 870–878, 2018.

[41] T. Kik, "Heat source models in numerical simulations of laser welding," *Materials*, vol. 13, no. 11, p. 2653, 2020.

[42] P. Promoppatum, S.-C. Yao, P. C. Pistorius, and A. D. Rollett, "A comprehensive comparison of the analytical and numerical prediction of the thermal history and solidification microstructure of Inconel 718 products made by laser powder-bed fusion," *Engineering*, vol. 3, no. 5, pp. 685–694, 2017.

[43] Mengel, Aaron, "Finite element modeling of LENS deposition using SYSWELD" (2002). Theses and Dissertations. Paper 750.

[44] Z. Chen, Y. Lu, F. Luo, S. Zhang, P. Wei, S. Yao, and Y. Wang, "Effect of laser scanning speed on the microstructure and mechanical properties of laser-powder-bed-fused K418 nickel-based alloy," *Materials*, vol. 15, no. 9, p. 3045, 2022.

[45] C. Jasien, A. Saville, C. G. Becker, J. Klemm-Toole, K. Fezzaa, T. Sun, T. Pollock, and A. J. Clarke, "In situ X-ray radiography and computational modeling to predict grain morphology in β-titanium during simulated additive manufacturing," *Metals*, vol. 12, no. 7, p. 1217, 2022.

[46] P.-F. Paradis, T. Ishikawa, and S. Yoda, “Non-contact measurements of thermophysical properties of niobium at high temperature.,” *Journal of Materials Science*, vol. 36, no. 21, pp. 5125–5130, 2001.

[47] F. Koechlin and B. Bonin, “Parametrization of the niobium thermal conductivity in the superconducting state,” *Superconductor Science and Technology*, vol. 9, no. 6, pp. 453–460, 1996.

[48] P. Kaur and C. Bera, “Effect of alloying on thermal conductivity and thermoelectric properties of CoAsS and CoSbS,” *Physical Chemistry Chemical Physics*, vol. 19, no. 36, pp. 24928–24933, 2017.

CHAPTER 3

SOLIDIFICATION BEHAVIOR OF REFRACTORY ALLOY C103 UNDER ADDITIVE MANUFACTURING CONDITIONS

A. Miklas[1], A. Deal[2], C. Lough[3], N. Phillips[2], J. Klemm-Toole[4], A.J. Clarke[4]

3.1 Abstract

C103 is a Nb-based refractory alloy that can perform at ultra-high temperatures (1200 - 1800°C). Additive manufacturing (AM) has emerged as an appealing fabrication method for C103 because it allows near net-shaped parts to be created with a tailored microstructure that requires little thermomechanical processing. In this study, the solidification behavior of C103 under AM conditions was examined for both single laser track melts and a completed laser powder bed fusion (LPBF) build. Corresponding solidification models were created for each set of AM conditions. The melt tracks were imaged in the scanning electron microscope (SEM) and it was determined that several melt tracks exhibited non-ideal behavior. Electron backscatter diffraction (EBSD) analysis of the melt tracks revealed that C103 exhibited primarily epitaxial growth with some new grain nucleation able to be observed along the centerline of melt tracks. The behavior in the melt tracks was found to be consistent with that of the completed build. The metallographic analysis was compared to the solidification models to predict the columnar to equiaxed transition (CET) behavior. It was ultimately determined that these models were not able to accurately predict the solidification behavior of the C103 under additive manufacturing conditions. This disparity was largely attributed to the input parameters for the solidification model, which were developed using Thermo-Calc and SYSWELD. These input parameters include the C103 specific Gibbs-Thomson coefficient and thermophysical properties, the solute specific liquidus slopes and partitioning coefficients, as well as the process specific thermal gradients. While the accuracy of all the input parameters was unable to be validated, each input parameter was evaluated to determine the likely changes required for the modeled values to generate solidification models that better correspond to what was observed experimentally.

3.2 Introduction

Refractory alloys first rose to prominence in the aerospace industry in the 1950s in support of turbine engine development. Since then, the focus of refractory alloys has largely shifted to application in nuclear and hypersonic propulsion systems [1]. Refractory alloys are attractive for these applications because of their ability to perform at ultra-high temperatures up to 1200 - 1800°C, which exceeds the capabilities of conventional superalloys. These temperature capabilities are of particular interest to the

---

[1] Author, performed most experimental work, participated in research planning

[2] Coauthor, helped with planning experiments and discussing results

[3] Performed single-track melts

[4] Project advisor, helped with planning experiments and discussing results

aerospace industry, because propulsion systems will work more efficiently, achieve higher speeds, and produce lower emissions when operated at higher temperatures. The temperature capabilities of the superalloys currently in use limit potential system gains, which makes refractory alloys, specifically C103, appealing for high temperature applications. C103 is a Nb-based refractory alloy that is today one of the prominent refractory alloys in the aerospace industry. C103 components can be operated at temperatures of 1200-1400°C [2].

C103 is currently used for components such as thrust augmenter flaps and rocket nozzles [2]. However, more extensive use of C103 is limited by its ability to undergo thermomechanical processing operations. Refractory alloys typically suffer from low room temperature ductility and a high oxygen affinity, which make them difficult and expensive to thermomechanically process by conventional methods [3]. Additive manufacturing (AM) is an attractive alternative production technique because it is performed in an inert gas environment that minimizes oxidation and is capable of producing a near net-shape part with a targeted microstructure, thereby minimizing the need for thermomechanical processing [4]. In addition to being a more efficient manufacturing method, C103 processed by AM has also been observed to display a higher strength than wrought material at both room and elevated temperatures, though the elongation is lower [1]. AM is currently utilized to manufacture C103 parts for reaction control system (RCS) thrusters, in-space propulsion systems, and hypersonics [5].

The applications of AM C103 can be expanded further by understanding how AM processing conditions affect the solidification behavior and the resultant microstructure. In this work, this behavior is systematically studied with processing variations. This was accomplished by performing single-track laser melts with AM equipment on samples of bulk material. The melt tracks were evaluated to reveal the melt pool and microstructure morphologies produced by different processing conditions, thereby providing a framework for the selection of scan strategies that are more ideal. Solidification models are valuable in predicting the microstructure evolution as it relates to scan strategies, so models were developed with available thermophysical property data and compared to experimentation. A completed C103 build was also evaluated and modeled to assess the applicability of single-track microstructure evaluation to a full build.

3.3 Experimental Procedures

A cast sample of single-phase, body-centered cubic (BCC) C103, composition is shown in Table 3.1 with an average grain size of 300 μm, which was made flat and parallel with the final surface being ground with 1200-grit sandpaper.

Table 3.1: Chemistry for as-cast C103, represented in weight percent, and measured using combustion for the C, inert gas fusion for the H, N, and O, and inductively coupled plasma (ICP) mass spectrometry for the remaining elements.

Element	Composition [wt. %]
C	< 0.01
H	0.001
Hf	9.99
N	< 0.01
Nb	88.14
O	0.01
Ti	1.02
Ta	< 0.01
W	0.02
Zr	0.78

Five laser track melts, as shown in Figure 3.1, were performed at the Kansas City National Security Campus (KCNSC) on their custom laser powder bed fusion (LPBF) machine in an argon gas atmosphere with less than 200 ppm oxygen at atomic pressure. The IPG Photonics AM-RAD LPBF machine utilized an IPG Photonics YLR-500 fiber laser. The laser power and speed combination used for each laser melt track were recommended by KCNSC to ensure that a variety of melt pool morphologies were produced, as detailed in Table 3.2.

Figure 3.1. Top-down macro image of the five melt tracks completed on the C103 sample. Each melt track is labelled 1-5 which corresponds to parameters detailed in Table 3.2.

The sample was sectioned in the middle of the tracks after top-down imaging was completed to target the steady-state region of each melt track. The cross sections of each melt pool were evaluated, and the bulk microstructures were characterized in a TESCAN S8000G scanning electron microscope (SEM). The melt pools were characterized with electron backscatter diffraction (EBSD) in an FEI Helios NanoLab 600i SEM equipped with an EDAX Hikari Super 1400pps EBSD detector, using a beam current of 11 nA, accelerating voltage of 20 kV, and working distance of approximately 26 mm. The base material, away from the melt pools, was also evaluated with energy dispersive spectroscopy (EDS) in the TESCAN, which was outfitted with an EDAX Octane Elect Plus EDS system, with beam currents ranging from 300 pA - 10 nA, accelerating voltages ranging from 10 kV – 25 kV, and a working distance of 6 mm. Solidification segregation behavior was predicted using Scheil simulations completed in Themo-Calc with the TCHEA5 database and compared to the EDS results [6].

A second sample of a completed C103 build was evaluated in the as-built condition in the same manner as the single laser melt tracks just described. This build was completed on a similar LPBF machine at ATI using an argon gas atmosphere. The laser conditions for this sample were in a similar range to what was used for the single melt tracks and are provided in Table 3.2 and designated with "AM." The AM sample was cut so that the cross sections of the laser melt tracks were evaluated. This sample was compared to the single-track melts to evaluate the applicability of the single-track analysis to inform AM of a completed build.

Table 3.2. Laser parameters used for each melt track shown in Figure 3.1 as well as the parameters used for the AM sample.

Parameter Set	**Power [W]**	**Speed [m/s]**	**Beam Diameter [µm]**	**Linear Energy Density [J/m]**
1	162	0.8	75	203
2	243	0.2	75	1215
3	162	0.5	75	324
4	405	1.7	75	238
5	324	1.7	75	191
AM	280	0.9	100	311

Thermal gradient simulations were completed using the commercial simulation software, SYSWELD. The heat transfer conditions were simulated considering only conductive heat transfer for each of the melt tracks. The temperature fields created by the heat transfer simulations were used to calculate thermal gradients. A C103 material file was created in SYSWELD using thermophysical properties modeled in Thermo-Calc; the density, thermal conductivity, and specific heat were modeled as functions of temperature using the TCHEA5 database. The modeled properties are shown at various temperatures ranging between the solid and liquid regions are depicted in Table 3.3. All three properties displayed an abrupt change at the liquidus temperature. To capture this, the predicted value at the liquidus temperature in the solid-liquid region as well as the predicted value at the liquidus temperature in the liquid region are both shown.

Table 3.3: CALPHAD thermophysical property predictions used to create the SYSWELD material files.

Thermophysical Property	**Room Temperature (in solid region)**	**Liquidus temperature in solid-liquid region**	**Liquidus temperature in liquid region**	**3000 K (in liquid region)**
Density [kg/m^3]	8.79E+03	8.24E+03	7.94E+03	7.78E+03
Specific Heat [J/kg-K]	261.46	416.04	427.65	435.02
Thermal Conductivity [W/m-K]	50.89	12.13	48.44	52.51

The melt pool shapes and sizes in the final simulations were representative of the experimental melt pool sizes within approximately 10%. The melt pools were identified in SYSWELD by measuring the region at or above the liquidus temperature, which was also modeled in Thermo-Calc. These final simulations were used to calculate the thermal gradient (G) and solidification velocity (V) at approximately five points at the solid-liquid interface between the top and bottom of the melt pool, along the tail, as shown in Figure 3.2.

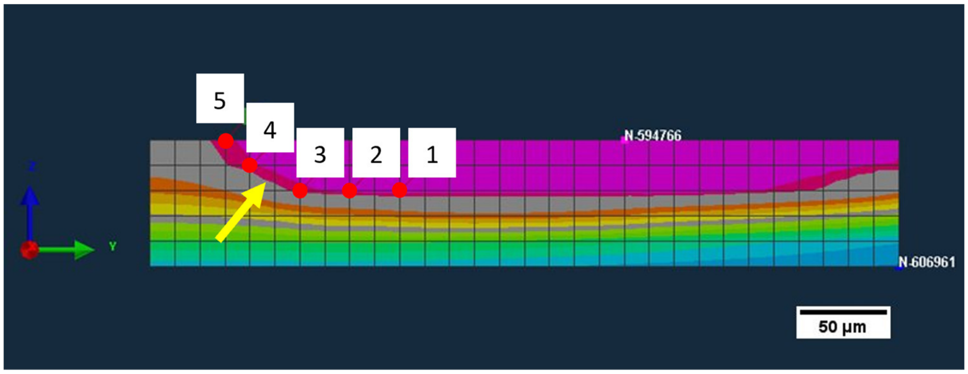

Figure 3.2. Locations of the thermal gradient and cooling rate measurements on the thermal contour map for melt track 5. The solid-liquid interface is represented by the grey-red interface, indicated with a yellow arrow. This is a longitudinal cross section that shows the melt pool traveling from left to right with measurements placed along the tail of the melt pool tail.

The total thermal gradient, G, at each point on the solid-liquid interface was calculated using Equation 3.1 where G_x, G_y, and G_z represent the thermal gradients in the x, y, and z directions. The corresponding solidification velocities, V, were calculated using the total thermal gradient and cooling rate, $\dot{C}$, with Equation 3.2 [7]. The simulated gradients and cooling rates were later used to create process curves for each melt track and AM processing conditions.

$$G = \sqrt{G_x^2 + G_y^2 + G_z^2} \tag{3.1}$$

$$V = \frac{\dot{C}}{G} \tag{3.2}$$

Solidification curves for C103 were created and combined with the process curves to predict the final microstructures present in the melt tracks. The process curves were created with the heat transfer simulation for each melt track, so they are not only alloy specific, but also specific to processing conditions. The solidification curves show the columnar to equiaxed transition (CET) which allows the final microstructures to be predicted. These CET predictions were based on a simplified version of the Kurz-Giovanola-Trivedi (KGT) dendrite growth model [8]. In this model, solute diffusivities D_i, partitioning coefficients k_i, and liquidus slopes m_i are assumed to be constant in addition to the Gibbs-Thomson coefficient Γ and initial liquid solute concentration, C_i, which are by nature constant. The Gibbs-Thomson coefficient and solute diffusivities were taken from literature while the partitioning coefficients and liquidus slopes were modeled in Thermo-Calc using the TCHEA5 database [9, 10]. The initial solute concentration is known from the alloy composition. These input parameters are shown in Table 3.4. The Gibbs-Thomson coefficient and solute diffusivities used for the model are experimental values for Ni and Ti-alloys, respectively. These values were selected because these alloy systems have similar high temperature capabilities to C103 and due to limited availability of refractory alloy data.

Table 3.4: Input parameters used for CET model.

Solute	**Parameter**	**Value**
	Gibbs-Thomson Coefficient [9]	1.92E-7 K*m
Hf	Diffusion Coefficient [10]	2.00E-9 m^2/s
	Partition Coefficient	0.57
	Liquidus Slope	-4.93 K/wt.%
	Initial Concentration	9.0 wt.%
Zr	Diffusion Coefficient [10]	2.00E-9 m^2/s
	Partition Coefficient	0.51
	Liquidus Slope	-9.34 K/wt.%
	Initial Concentration	0.7 wt.%
Ti	Diffusion Coefficient [10]	2.00E-9 m^2/s
	Partition Coefficient	0.58
	Liquidus Slope	-14.91 K/wt.%
	Initial Concentration	0.7 wt.%

To calculate the tip radius R, with Equation 3.7, the Peclet number P_i, and the liquid solute concentration at the dendrite tip C_i^*, and ξ_i are first calculated with Equations 3.3, 3.4, and 3.6, respectively [8].

$$P_i = \frac{L_i v_i}{D_i} \tag{3.3}$$

$$C_i^* = \frac{C_o}{1 - [(1 - k_i) Iv(P_i)]} \tag{3.4}$$

The Peclet number is dependent on the fluid velocity v_i, the characteristic length of the system L_i, and the diffusion coefficient while the solute concentration at the dendrite tip is dependent on the initial liquid solute concentration, the partitioning coefficient, and the Ivantsov function $v(P_i)$ [11]. The Ivantsov function, in which E_1 represents the exponential integral, is shown in Equation 3.5. Equation 3.6 shows ξ_i, which is a function of the Peclet number [9]. In addition to these calculated values, Equation 3.7 also utilizes the simulated solidification thermal gradient G to calculate the tip radius. The solidification velocity V is calculated with Equation 3.8.

$$Iv(P_i) = P_i e^{P_i} * E_1(P_i) \tag{3.5}$$

$$\xi_i = 1 - \frac{2k_i}{\sqrt{1+\left(\frac{2\pi}{P_i}\right)^2} - 1 + 2k_i} \tag{3.6}$$

$$4\pi^2\Gamma\left(\frac{1}{R^2}\right) + \left(2\sum[m_i P_i(1-k_i)C_i^*\xi_i]\right)\left(\frac{1}{R}\right) + G = 0 \tag{3.7}$$

$$V = \frac{2P_i D_i}{R} \tag{3.8}$$

Equations 3.7, 3.8, and 3.9 are used to calculate the solute undercooling $\Delta T_{c,i}$, the curvature ΔT_r, and the total undercooling ΔT_{total}, respectively. The undercooling plots created with these equations show both total undercooling for the alloy as well as undercooling for each individual constituent, which can be useful in guiding the selection of future alloy compositions [8].

$$\Delta T_{c,i} = m_i(C_o - C_i^*) \tag{3.9}$$

$$\Delta T_r = \frac{2\Gamma}{R} \tag{3.10}$$

$$\Delta T_{total} = \sum_i \Delta T_{c,i} + \Delta T_r \tag{3.11}$$

The total undercooling was plotted as a function of solidification velocity and the curve was fit with a power law model represented in Equation 3.12, to determine the material constants a and n. These are then used in Equation 3.13 to compute G and complete the CET model. In Equation 3.13, N_o is the nucleation site density, Φ is the volume fraction of equiaxed grains, and ΔT_n is the nucleation undercooling. Both the nucleation site density and the nucleation undercooling used in this model were taken from Ni-alloy experimentation because there is limited data available for refractory alloys and the Ni-alloy has similar high temperature capabilities to C103 [12].

$$\Delta T = (a * V)^{1/n} \tag{3.12}$$

$$G = \frac{1}{n+1} * \left(\frac{-4\pi N_o}{3\ln(1-\Phi)}\right)^{\frac{1}{3}} * \left(1 - \frac{\Delta T_n{}^{n+1}}{(a * V)^{\frac{n}{n+1}}}\right) * (a * V)^{\frac{1}{n}} \tag{3.13}$$

The CET model is comprised of curves representing both a microstructure with 1% equiaxed grains and one with 50% equiaxed grains. When the predicted microstructure falls below the 1% equiaxed line, the microstructure is said to be columnar while it is said to be equiaxed when the predicted microstructure falls above the 50% equiaxed line. These two curves are created by calculating the thermal gradient with volume fractions of 0.0066 and 0.49, respectively. The predicted thermal gradient for solidification processes is expected to be high, which means that the grains will likely be elongated to a degree regardless of the microstructure predicted with the CET model.

3.4 Results

Each melt track was imaged in the top-down orientation with the melt tracks moving from left to right, shown in Figure 3.3a – e. No surface cracking was observed. Cross-sectional images are also included in Figure 3.3f – j of the melt tracks imaged using the backscatter detector to better display the melt pool morphology [13]. The melt pools are outlined with a dashed yellow line. Melt tracks 1 and 3 were both completed using the lowest power but track 3 used a slower scan speed and thus a higher linear energy density. As a result, they display similar behavior in the top-down orientation but track 3 is both wider and deeper than track 1. The highest linear energy density was used to create track 2, which appears widest in the top-down orientation and exhibits keyhole behavior in the cross section. Tracks 4 and 5 were produced with the highest speed, which ultimately caused balling to occur, indicated with blue arrows in Figures 3.3d and e. Track 4 used the higher power of the two tacks and was therefore wider and deeper than track 5. The AM sample, the cross-section of which is shown in Figure 3.4a, used a linear energy density most similar to track 3. The melt pool size was approximated in the cross-sectional image and found to be similar to track 3 in width but almost twice as deep.

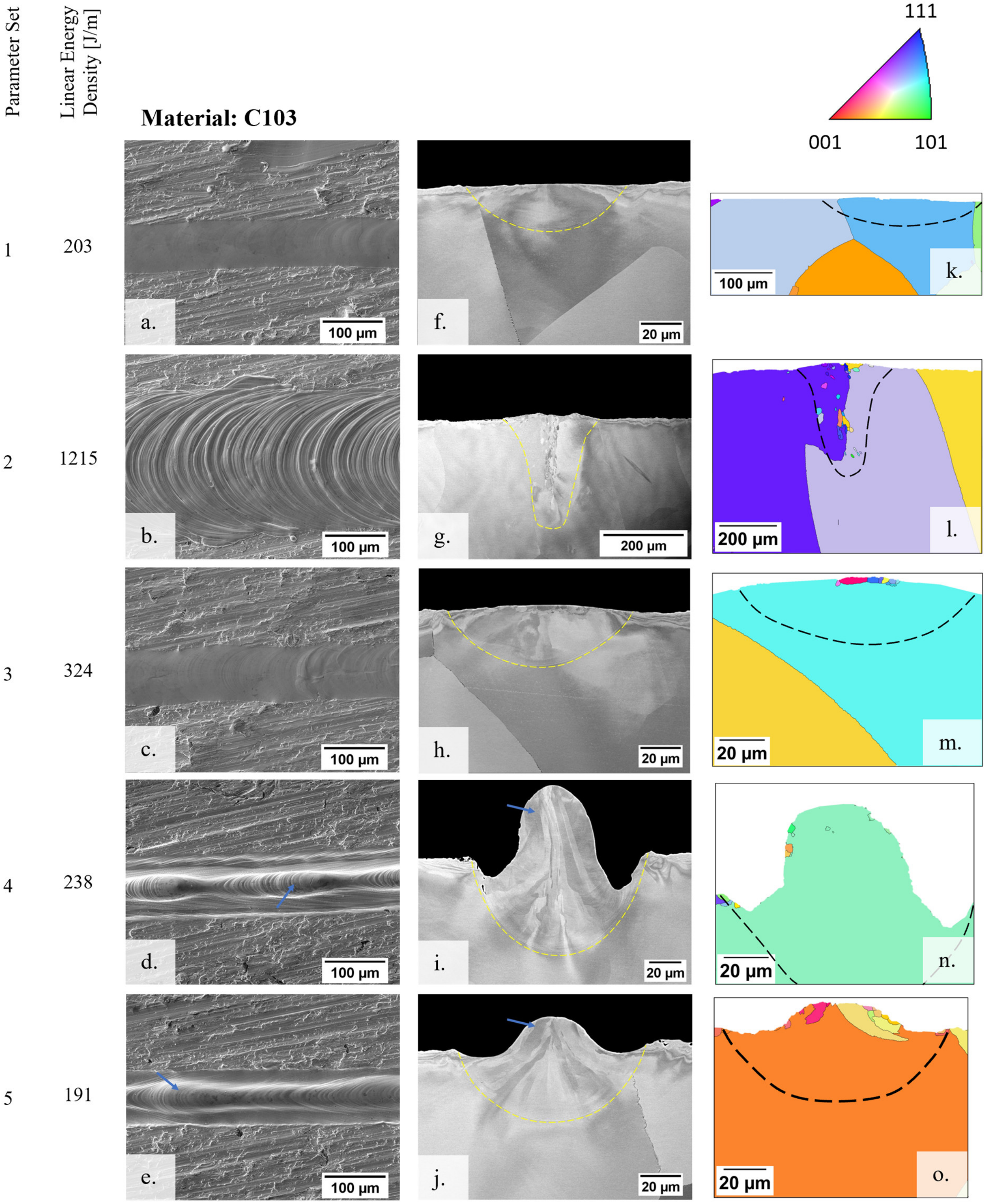

Figure 3.3. Top-down images of each melt track are represented in a. – e., cross-sectional micrographs are shown in f. – j. and IPF maps are shown in k. – o. The corresponding melt track parameters are shown to the left of the images and the IPF map key is shown above the IPF maps.

The inverse pole figure (IPF) maps created with EBSD of each track are also shown in Figures 3.3k – o next to the corresponding micrograph. The C103 exhibited primarily epitaxial growth with some new grain nucleation able to be observed along the centerline of melt tracks 2, 3, and 5, as shown in Figures 3.3l, m, and o, respectively. Melt tracks 1 and 4, displayed in Figures 3.3k and n, respectively, both exhibited little to no new grain nucleation. Figure 3.4b shows the IPF map of the AM sample, which displayed both new grain nucleation and epitaxial growth. This structure has been observed in LPBF-processed C103; grain growth parallel to the build direction with overlap occurring between adjacent melt pools [14].

The melt tracks were evaluated a second time in the top-down orientation after being polished to establish any influence the dendritic structure in the cast base material may have had on the melt track. The melt tracks displayed consistent behavior for the length of each track, indicating that the dendrites did not influence the tracks.

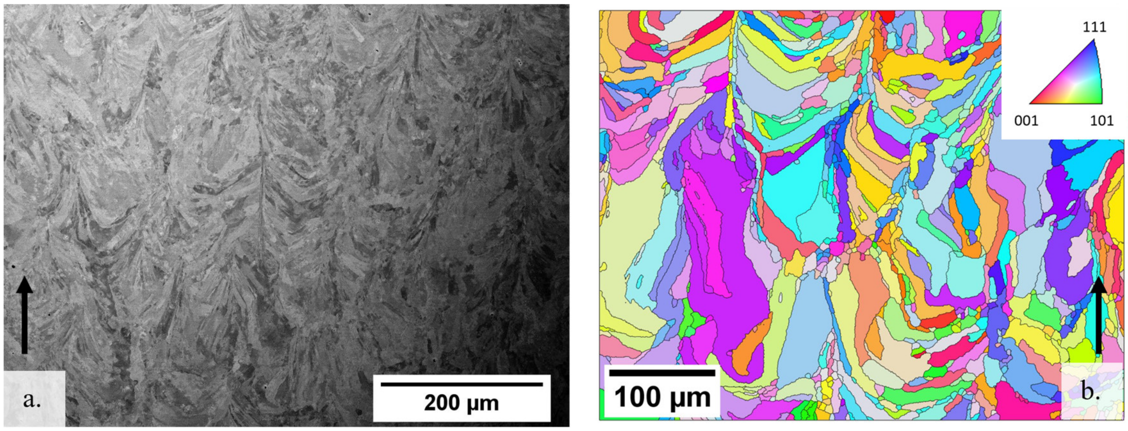

Figure 3.4. Cross-sectional backscatter image (a.) and IPF map (b.) of the AM sample with the build direction going upward.

A Scheil simulation was performed for C103 to predict the solidification segregation behavior, shown in Figure 3.5a. The four elements with the largest weight percent contribution were selected to be included in the simulation. The Nb was predicted to be rich in the first solid to form and depleted in the last while the Hf, Zr, and Ti were predicted to be depleted in the first solid to form and the richest in the last. This indicates that the Nb will segregate to the dendrite cores while the Hf, Zr, and Ti will segregate to the interdendritic regions.

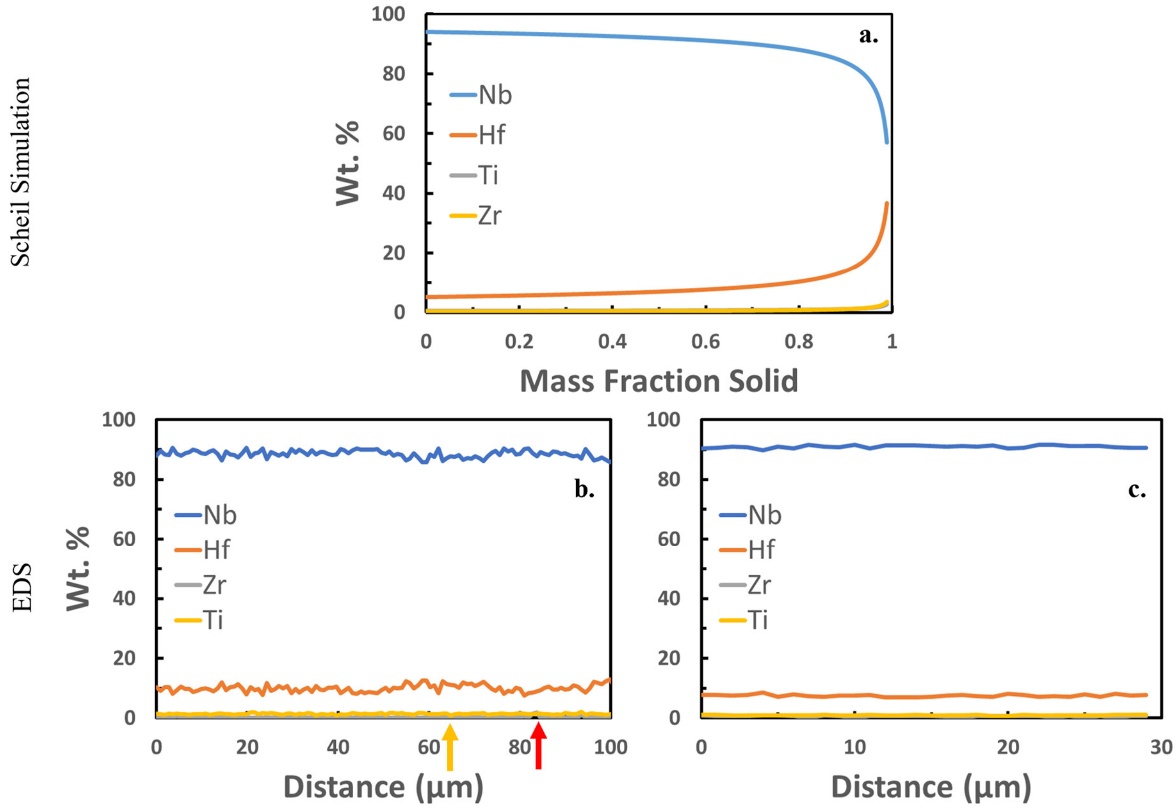

Figure 3.5. Scheil simulations for C103 (a.) and the EDS line scans for the bulk, as-cast material (b.) and AM sample (c.). The dendritic region in (b.) is indicated with a red arrow while the interdendritic is indicated with a yellow arrow.

EDS measurements were taken in the bulk of both the as-cast and AM samples. This was done to evaluate the segregation behavior and relate this to the simulated behaviors. In the as-cast condition, the bulk scans targeted grain boundaries and dendrites. In the AM sample, the scans targeted the melt pools. Line scans were also taken within each melt track in the as-cast material. No variation was observed across grains and very little was observed across dendrites. No variation was observed either in the AM sample, shown in Figure 3.5, or in the melt tracks. However, while the EDS detector used can detect variation in the base material, it likely does not have an energy resolution capable of detecting elemental segregation within the melt pools. A scan of the as-cast bulk material is shown in Figure 3.5b where an interdendritic region is present at approximately 65 µm, indicated with a yellow arrow, and a dendrite core is present at approximately 85 µm, indicated with a red arrow. Slight variation was seen for the Nb and Hf, which have the highest compositional contribution to the alloy, at the dendrite core. No variation was observed in the Zr or Ti. The apparent variations agreed with the Scheil simulations. A scan of a melt pool in the AM sample, which exhibited no variation, is shown in Figure 3.5c. The AM sample was expected to exhibit less severe partitioning than the as-cast sample. In a study conducted on LPBF-processed C103, it was found that the fast solidification rate inherent to the LPBF process prevented micro-segregation. This is desirable because it contributes to a small grain size distribution that improves the strength of the C103 so that it surpasses even wrought material [14].

The solidification maps created for each set of laser conditions used are shown in Figure 3.6, depicting the 1% and 50% equiaxed curves. These were combined with the process curves created from the SYSWELD simulations, also shown in Figure 3.6. The SYSWELD simulations were created using the experimental laser processing parameters to simulate the melt pool widths and depths measured in Figures 3.3 and 3.4. The measured and simulated melt pool widths and depths are depicted in Table 3.5.

Table 3.5: Measured and simulated melt track widths and depths for each parameter set and the AM sample.

Parameter Set	**Linear Energy Density [J/m]]**	**Measured**		**Modeled**	
		Width [µm]	**Depth [µm]**	**Width [µm]**	**Depth [µm]**
1	203	77	22	66	18
2	1215	236	215	212	181
3	324	91	28	78	23
4	238	110	59	102	58
5	191	91	36	84	33
AM	311	93	60	90	57

The bottom point in each curve corresponds to the bottom of the melt pool and the top point in each curve corresponds to the top of the melt pool. This is shown schematically in Figure 3.2 where points 1 and 5 show the location of the measurements taken at the bottom and top of the melt pool, respectively. While each process curve exhibits a similar shape, melt tracks 4 and 5 display the highest thermal gradients, which corresponds to the experimental process parameters. A summary of the experimental results and predicted results is depicted in Table 3.6.

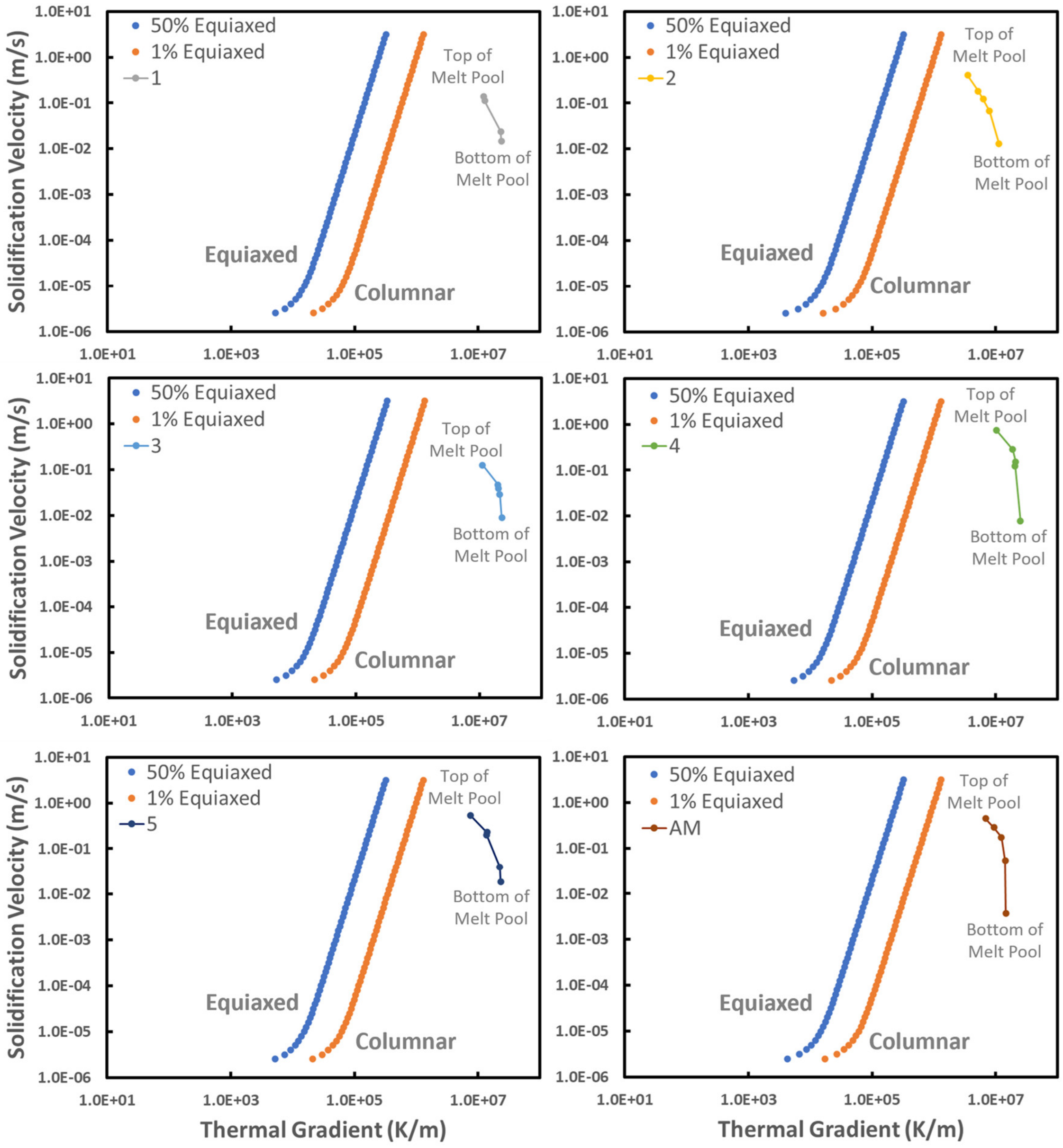

Figure 3.6. CET solidification map for each melt track and AM sample.

Table 3.6: Summary of the experimental results and predicted results.

Parameter Set	Linear Energy Density [J/m]]	Experimental	Calculated
1	203	Only epitaxial growth observed	Columnar
2	1215	Equiaxed	Columnar
3	324	Equiaxed	Columnar
4	238	Equiaxed	Columnar
5	191	Equiaxed	Columnar
AM	311	Mixed	Columnar

3.5 Discussion

The top-down and cross-sectional images revealed deleterious keyholing behavior in track 2 and balling in tracks 4 and 5. The keyhole shape of track 2 indicates that the melt pool depth is no longer controlled by conduction only, which will affect the simulation behavior for this track [15]. Keyholing has been found to be most directly affected by the energy density of the laser conditions used in single track melts performed with an LPBF machine on stainless steel ; the laser conditions used for melt track 2 produced the highest linear energy density observed in this study [16]. Tracks 4 and 5 were both created with the highest speed used in this study. Balling occurs when breaks appear in the melt track, which is undesirable in AM. It is caused by high laser scan speeds that create instability in the melt pool. This instability, known as the Rayleigh instability, is the result of the high ratio between the length and width of the melt pool and is resolved when the melt pool breaks to lower the surface energy of the system [17]. Balling can cause defects or even build failures in a full build [18]. The AM sample did not display any balling-related build defects. The presence of keyholing and balling in these three tracks indicates the parameters used for tracks 1 and 3 are more ideal for AM of C103. This is confirmed by the AM sample, which used a linear energy density close to that of track 3; this parameter combination was used to create a successful build.

The IPF maps showed both epitaxial growth and heterogeneous nucleation in the melt tracks. The heterogeneous nucleation occurred primarily at the centerline of each melt pool. This behavior can be attributed to the total undercooling of the system at different points in the melt pool because the total undercooling dictates the initiation of heterogeneous nucleation. The total undercooling is expected to be low at the bottom of the melt pool and high at the top of the melt pool. As a result, at the bottom of the melt pool there is very little driving force for heterogeneous nucleation and grains are expected to grow epitaxially while at the top, the driving force is increased so heterogeneous nucleation is expected [19].

The IPF map of the AM sample shows some epitaxial growth between adjacent melt pools and columnar growth that is parallel to the build direction. This is consistent with the epitaxial growth observed in the track 3, which was created with the linear energy density most like that used for the AM sample. Grains growing epitaxially in the build direction are expected in this orientation. This somewhat columnar structure with new grain nucleation in the melt pools has been observed for this orientation in both as-built samples and stress relieved samples of C103 [2, 14].

Solidification curves for each processing parameter set were created and paired with their respective process curves to generate a solidification map and predict the CET behavior and final microstructure of each melt track. This prediction method has been used to successfully model the behavior of Al-alloys under LPBF conditions, which indicates that the modeling procedure can generate accurate predictions [20]. The behavior of the process curves relative to one another can be compared to the laser parameters used experimentally. The solidification velocity at the top of the melt pool is expected to be representative of the scan speed. This has been observed in Ni-based superalloy heat transfer modeling as well [21]. A difference of about two orders of magnitude is expected between the top and bottom solidification velocities, with the bottom solidifying more slowly. This generally holds true for these predictions, which show tracks 4 and 5 as having the highest solidification velocity at the top of the melt pool. The AM sample displays the next highest solidification velocity, which is expected. This is expected because solidification velocity has been found to be directly related to laser scan speed [22]. However, while track 3 displays a solidification velocity at the top of the melt pool that is expected based on the scan speed, track 1 displays a lower-than-expected solidification velocity, indicating that the simulation is lacking for this track. Track 2 also does not follow this trend and displays a slightly different shape than the other curves. This can be attributed to the keyholing behavior. Because the melt pool is no longer controlled solely by conduction when operating in "keyhole mode," SYSWELD, which only accounts for conductive heat transfer, is not sufficient to fully characterize the track. Further simulations should be completed for track 2 with a program that also takes convective heat transfer into account to characterize the system more accurately. Additionally, the smaller tracks like 1 and 3 had difficulty in the simulations due to the minimum mesh size of SYSWELD. SYSWELD is a good tool for creating rough estimates and observing general trends but a tool that can achieve a finer mesh and therefore more precision in its simulations should be used. One such alternative program is FLOW-3D, which has successfully modeled the heat transfer behavior of steel processed via LPBF with similar laser conditions [23]. It has also been used to successfully model keyhole behavior in an LPBF-processed Ti-alloy [24].

All the solidification maps generally follow the same shape, which indicates that the shape is not process-dependent but thermomechanical property-dependent. The maps predict that tracks 4 and 2 will display some equiaxed grains at the top of the melt pool, but the other melt tracks and the AM sample are predicted to be completely columnar. This is not consistent with experimental results. This inconsistency is largely attributed to the heat transfer simulations and the thermophysical property modeling that supplemented it.

This was determined by calculating the primary dendrite arm spacing (PDAS) from the models and comparing that to the measured PDAS. A similar comparison method was used to assess the heat transfer modeling of a Ni-based superalloy. In that analysis, the PDAS was predicted for various single laser track melts at several points along the melt pool. The measured values were found to align with the calculated values [25]. The measured and calculated PDAS for C103 at the bottom of the melt pool are shown in Table 3.8. An image of one of the areas used to create the PDAS measurements is shown in Figure 3.7. The yellow line spans approximately ten dendrites. Several similar measurements were made in each melt pool and AM sample to calculate the average values reflected in Table 3.8. A similar average PDAS measurement method was employed in a separate study evaluating LPBF-processed steel [26].

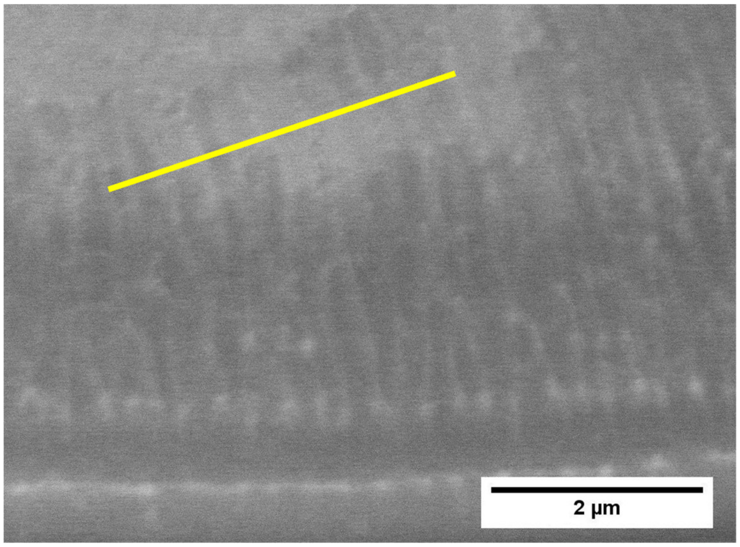

Figure 3.7. Backscatter image of track 3 showing primary dendrites near the bottom of the melt pool. The yellow line indicates an example measurement area.

The PDAS was calculated with Equation 3.14, where λ represents PDAS. The tip radius, R, is plotted as a function of solidification velocity as part of the KGT model. This plot is fitted with a power law model, as shown in Equation 3.15, in which α and β are constants taken from the fit model. The non-equilibrium freezing range $\Delta T_o'$, is calculated with Equation 3.16, in which T_{tip} represents the liquidus temperature modeled in Thermo-Calc and T_{base} represents the non-equilibrium solidus temperature, which is taken from the Scheil simulations. The modeled thermal gradient is represented by G. The melt track specific thermal gradient that was modeled in SYSWELD was used to generate PDAS predictions for each set of laser conditions. The calculated and measured PDAS are expected to differ only slightly (less than an order of magnitude) if the input parameters are representative of experimentation. However, the calculated and measured values were found to differ by approximately an order of magnitude, as shown in Table 3.8, indicating that the input parameters could be the source of the observed inconsistency [27].

$$\lambda = \sqrt{\frac{3R\Delta T_o'}{G}} \tag{14}$$

$$R = \alpha V^{\beta} \tag{15}$$

$$\Delta T_o' = T_{tip} - T_{base} \tag{16}$$

The Gibbs-Thomson coefficient is used as an input parameter in the KGT model from which tip radius is predicted. A C103-specific coefficient was unable to be determined so a Ni-alloy coefficient was used in the model. To test the effect of the Gibbs-Thomson coefficient, Γ, on the solidificaiton map, the minimum and maximum allowable coefficients were approximated for C103 with Equation 3.15 [17]. This method was successfully employed to calculate the Gibbs-Thomson coefficient in several high entropy alloys (HEAs) [28]. In this equation, T_m represents the melting temperature, γ_{sl} the solid-liquid interfacial energy, V_m the molar volume, and L_m the latent heat of fusion. T_m and V_m were calculated for C103 while L_m for pure Nb was taken from Smithells Metal Reference Book [29]. The interfacial energy was varied between minimum and maximum values to calculate the subsequent minimum and maximum Gibbs-Thomson coefficient. The input parameters and estimated Gibbs-Thomson coefficients are shown in Table 3.7.

Table 3.7: Estimated minimum and maximum Gibbs-Thomson coefficient, including input parameters.

T_m [K]	V_m [m^3/mol]	L_m [J/mol] [19]	γ_{sl} [J/m^2] [27]	Γ [K-m]
2639	1.1E-05	35600	0.03	2.95E-08
			0.3	2.95E-07

These coefficients were used to calculate theoretical PDAS, which generally varied by less than an order of magnitude, as shown in Table 3.8. There is some variability observed in these results because the minimum and maximum Gibbs-Thomson coefficients are approximated. As a result, it was concluded that the Ni-alloy coefficient used to create the solidification curves was not the source of the observed inconsistency.

$$\Gamma = \frac{T_m * \gamma_{sl} * V_m}{L_m} \tag{15}$$

Table 3.8: Measured PDAS compared to the PDAS calculated with the literature and estimated Gibbs-Thomson coefficients. PDAS calculated using the Rosenthal model is also included.

Parameter Set	Linear Energy Density [J/m]]	Measured PDAS [m]	PDAS Calculated with Ni-alloy Γ [m]	PDAS Calculated with Minimum Γ [m]	PDAS Calculated with Maximum Γ [m]	PDAS Calculated with Rosenthal model [m]
1	203	2.3E-07	2.8E-06	1.7E-06	2.1E-06	1.0E-06
2	1215	4.9E-07	4.3E-06	4.3E-06	4.5E-06	1.7E-06
3	324	2.7E-07	3.0E-06	1.9E-06	7.1E-06	1.3E-06
4	238	3.4E-07	3.0E-06	1.9E-06	2.2E-06	1.1E-06
5	191	2.8E-07	2.7E-06	1.7E-06	2.0E-06	1.0E-06
AM	311	4.1E-07	2.9E-06	1.8E-06	3.5E-06	1.1E-06

The liquidus slope and partitioning coefficient were also input parameters in the KGT model that were predicted in Thermo-Calc. There is not currently enough experimental data for C103 to validate these modeled parameters. However, their effect on the tip radius and thus the calculated PDAS can be evaluated. It was determined that a higher liquidus slope and a partitioning coefficient further from one would both result in a lower predicted tip radius and a lower predicted PDAS, bringing the calculated results closer to the measured results. This relationship has been shown to apply to both stainless steels and Ni-based superalloys [30].

The non-equilibrium freezing range was also modeled using CALPHAD databases. The predicted freezing range is higher than expected at 343 °C. Non-equilibrium freezing ranges calculated for Ni-based superalloys, which are often used as a point of comparison for refractory alloys, have been found to range from 265 - 285 °C [31] Similar overestimates have been observed in a study comparing the measured and modeled freezing ranges of various steels [32]. The modeled liquidus temperature was able to be validated with experimental data, but the non-equilibrium solidus was not. An increase in the predicted solidus would result in a lower calculated PDAS [33].

The modeled thermal gradient and solidification velocities are taken from SYSWELD simulations. SYSWELD utilizes a normally distributed heat source for its calculations [34]. Applying a Rosenthal model instead, which utilizes a point heat source, predicts a higher thermal gradient that can be considered the highest reasonable value [35]. However, it has been determined in heat transfer modeling of steel that SYSWELD creates a more realistic simulation and thermal gradient [36]. The higher predicted thermal gradients generated by the Rosenthal model result in smaller calculated PDAS values that are closer to the measured PDAS, though they are still inaccurate. This indicates that factors outside the thermal gradient must contribute to the inaccuracy of the microstructure predictions.

The material files used to generate the SYSWELD simulations also impacted the process curves. The modeled thermal conductivity specifically exhibited unexpected and unrealistic behavior. Pure Nb was modeled as a point of comparison because that system is relatively well-established; the density, specific heat, and thermal conductivity have all been measured in previous studies [37, 38, 39]. Both curves are shown in Figure 3.8. The thermal conductivity of C103 was expected to be lower than that of pure Nb and the shapes of the curves were expected to be similar [40]. However, the modeled C103 curve varies greatly from the pure Nb curve. The modeled C103 thermal conductivity was also compared to measured values of C103 thermal conductivity at lower temperatures and found to be inaccurate, which indicates that the property modeling completed with the current CALPHAD database is not sufficient to accurately characterize the C103 system.

To generate more accurate simulations, experimental thermal conductivity data for C103 bar stock provided by ATI was used in combination with the modeled pure Nb behavior to extrapolate a new theoretical thermal conductivity curve. The experimental data and extrapolated curve are shown in Figure

3.8. The extrapolated thermal conductivity was used to produce the process curves presented in Figure 3.6.

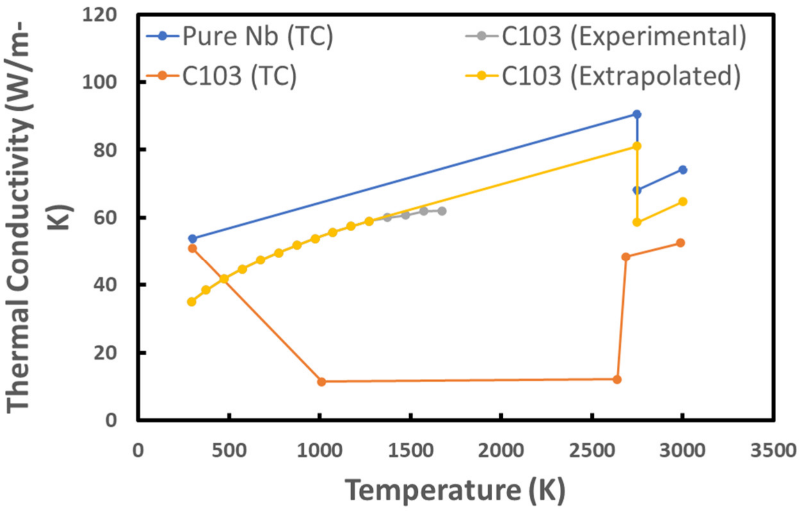

Figure 3.8. Thermal conductivity for C103 and pure Nb modeled in Thermo-Calc, experimental data for C103, and the extrapolated curve for C103.

3.6 Conclusions

This investigation was successful in showing that the melt pool morphologies and final microstructures are affected by the laser parameters, indicating that tailored microstructures can be achieved by manipulating the laser parameters. This evaluation of the single tracks in combination with the AM sample can thus be used to guide laser parameter selection; the parameter sets used for tracks 2, 4, and 5 (linear energy density: 1215, 238, and 191 J/m) were not ideal for creating a full build. The AM parameters (linear energy density: 311 J/m) were most similar to the parameters used for track 3 (linear energy density: 324 J/m) and the grain morphology of the full build was represented by that observed in track 3. It can therefore be concluded that the evaluation of the single tracks can be applied to full builds.

This investigation also showed that the current databases were successful in predicting the trends of the process curves should follow based on experimental laser parameters. However, the solidification and process curves were unable to accurately predict the resultant microstructure. It can therefore be assumed that there is some error in the modeled material properties (i.e., liquidus slope, partitioning coefficient, thermophysical properties). Such inconsistencies are exhibited in the comparison of the modeled and experimental thermal conductivity. However, most of these modeled values are unable to be validated with actual data. The likely shifts in the modeled values that will occur to make the solidification model more accurate are able to be predicted, however.

It can therefore be concluded that further characterization of C103, including the liquidus slope, partitioning coefficient, and thermophysical properties, should be completed to allow the solidification behavior to be accurately predicted.

3.7 Acknowledgements

Thank you to ATI Specialty Alloys and Components for providing material and material data in support of this project. This work was funded by the Department of Energy's Kansas City National Security Campus (KSCNC) which is operated and managed by Honeywell Federal Manufacturing Technologies, LLC under contract number DE-NA0002839. Thank you also to Sandia National Laboratories for their support. Sandia National Laboratories is a multimission laboratory managed and operated by National Technology and Engineering Solutions of Sandia LLC, a wholly owned subsidiary of Honeywell International Inc. for the U.S. Department of Energy's National Nuclear Security Administration under contract DE-NA0003525. This paper describes objective technical results and analysis. Any subjective views or opinions that might be expressed in the paper do not necessarily represent the views of the U.S. Department of Energy or the United States Government. Lab facilities at KCNSC, ATI, and Colorado School of Mines were used to support this work. This research used resources of the TESCAN S8252G RAMAN-SEM/FIB at the Colorado School of Mines which was acquired through the support of the National Science Foundation (DMR-1828454). I appreciate the contributions of Alec Saville, Chris Jasien, Megan Le Corre, Nate Peterson, Zane Fisher, and Gabriel Thompson.

3.8 References

[1] N. R. Philips, M. Carl, and N. J. Cunningham, "New opportunities in refractory alloys," *Metallurgical and Materials Transactions*, vol. 51, no. 7, pp. 3299–3310, 2020.

[2] P. D. Awasthi, P. Agrawal, R. S. Haridas, R. S. Mishra, M. T. Stawovy, S. Ohm, and A. Imandoust, "Mechanical properties and microstructural characteristics of additively manufactured C103 niobium alloy," *Materials Science and Engineering: A*, vol. 831, p. 142183, 2022.

[3] Y. Zhang and Q. Xing, "High entropy alloys: Manufacturing Routes," *Encyclopedia of Materials: Metals and Alloys*, pp. 327–338, 2022.

[4] J. M. Torralba and M. Campos, "High entropy alloys manufactured by Additive Manufacturing," *Metals*, vol. 10, no. 5, p. 639, 2020.

[5] P. R. Gradl, O. R. Mireles, and N. Andrews, "Introduction to Additive Manufacturing for Propulsion and Energy Systems," *AIAA Propulsion and Energy 2020*.

[6] Thermo-Calc Software, TCHEA version 5.1, January 2022.

[7] S. Bontha, N. W. Klingbeil, P. A. Kobryn, and H. L. Fraser, “Thermal process maps for predicting solidification microstructure in laser fabrication of thin-wall structures,” *Journal of Materials Processing Technology*, vol. 178, no. 1-3, pp. 135–142, 2006.

[8] W. Kurz, B. Giovanola, and R. Trivedi, “Theory of microstructural development during Rapid Solidification,” *Acta Metallurgica*, vol. 34, no. 5, pp. 823–830, 1986.

[9] M. Haines, A. Plotkowski, C. L. Frederick, E. J. Schwalbach, and S. S. Babu, “A sensitivity analysis of the columnar-to-equiaxed transition for ni-based superalloys in electron beam additive manufacturing,” *Computational Materials Science*, vol. 155, pp. 340–349, 2018.

[10] M. R. Rolchigo and R. LeSar, “Modeling of binary alloy solidification under conditions representative of Additive Manufacturing,” *Computational Materials Science*, vol. 150, pp. 535–545, 2018.

[11] R. Prichard, M. Gibson, C. Joseph, and W. Strasser, “A review of fluid flow in and around the brain, modeling, and abnormalities,” *Multiscale Biomechanical Modeling of the Brain*, pp. 209–238, 2022.

[12] M. Gäumann, C. Bezençon, P. Canalis, and W. Kurz, “Single-crystal laser deposition of superalloys: Processing–microstructure maps,” *Acta Materialia*, vol. 49, no. 6, pp. 1051–1062, 2001.

[13] *Standard Practice for Microetching Metals and Alloys*, ASTM E407-07(2015)e1, December 2016.

[14] O. Mireles, O. Rodriguez, Y. Gao, and N. Philips, “Additive manufacture of refractory alloy C103 for propulsion applications,” *AIAA Propulsion and Energy 2020 Forum*, 2020.

[15] W. E. King, H. D. Barth, V. M. Castillo, G. F. Gallegos, J. W. Gibbs, D. E. Hahn, C. Kamath, and A. M. Rubenchik, “Observation of keyhole-mode laser melting in laser powder-bed fusion additive manufacturing,” *Journal of Materials Processing Technology*, vol. 214, no. 12, pp. 2915–2925, 2014.

[16] W. Wang, J. Ning, and S. Y. Liang, “Analytical prediction of Balling, lack-of-fusion and keyholing thresholds in Powder Bed Fusion,” *Applied Sciences*, vol. 11, no. 24, p. 12053, 2021.

[17] A. V. Gusarov, I. Yadroitsev, P. Bertrand, and I. Smurov, “Heat transfer modelling and stability analysis of selective laser melting,” *Applied Surface Science*, vol. 254, no. 4, pp. 975–979, 2007.

[18] M. Król and T. Tański, “Surface Quality Research for selective laser melting of ti-6al-4v alloy,” *Archives of Metallurgy and Materials*, vol. 61, no. 3, pp. 1291–1296, 2016.

[19] P. Liu, Z. Wang, Y. Xiao, M. F. Horstemeyer, X. Cui, and L. Chen, “Insight into the mechanisms of columnar to equiaxed grain transition during metallic additive manufacturing,” *Additive Manufacturing*, vol. 26, pp. 22–29, 2019.

[20] S. Liu, H. Zhu, G. Peng, J. Yin, and X. Zeng, “Microstructure prediction of selective laser melting alsi10mg using finite element analysis,” *Materials & Design*, vol. 142, pp. 319–328, 2018.

[21] Y. Lee, M. Nordin, S. S. Babu, and D. F. Farson, “Effect of fluid convection on dendrite arm spacing in laser deposition,” *Metallurgical and Materials Transactions*, vol. 45, no. 4, pp. 1520–1529, 2014.

[22] Z. Chen, Y. Lu, F. Luo, S. Zhang, P. Wei, S. Yao, and Y. Wang, “Effect of laser scanning speed on the microstructure and mechanical properties of laser-powder-bed-fused K418 nickel-based alloy,” *Materials*, vol. 15, no. 9, p. 3045, 2022.

[23] P. Ninpetch, P. Kowitwarangkul, S. Mahathanabodee, R. Tongsri, and P. Ratanadecho, “Thermal and melting track simulations of laser powder bed fusion (L-PBF),” *IOP Conference Series: Materials Science and Engineering*, vol. 526, no. 1, p. 012030, 2019.

[24] M. Bayat, A. Thanki, S. Mohanty, A. Witvrouw, S. Yang, J. Thorborg, N. S. Tiedje, and J. H. Hattel, “Keyhole-induced porosities in laser-based powder bed fusion (L-PBF) of ti6al4v: High-fidelity modelling and experimental validation,” *Additive Manufacturing*, vol. 30, p. 100835, 2019.

[25] Y. Lee, M. Nordin, S. S. Babu, and D. F. Farson, “Effect of fluid convection on dendrite arm spacing in laser deposition,” *Metallurgical and Materials Transactions*, vol. 45, no. 4, pp. 1520–1529, 2014.

[26] Y. Tian, R. Palad, and C. Aranas, “Microstructural evolution and mechanical properties of a newly designed steel fabricated by laser powder bed fusion,” Additive Manufacturing, vol. 36, p. 101495, 2020.

[27] J. A. Dantzig and M. Rappaz, Solidification, 2nd Edition. Lausanne, Suisse: EPFL Press, 2016.

[28] D. J. Ferreira, B. N. Bezerra, M. N. Collyer, A. Garcia, and I. L. Ferreira, “The use of computational thermodynamics for the determination of surface tension and Gibbs–Thomson coefficient of multicomponent alloys,” *Continuum Mechanics and Thermodynamics*, vol. 30, no. 5, pp. 1145–1154, 2018.

[29] “Thermochemical Data,” Smithells Metals Reference Book, 2004.

[30] J. J. Blecher, T. A. Palmer, and T. DebRoy, “Solidification map of a nickel-base alloy,” *Metallurgical and Materials Transactions*, vol. 45, no. 4, pp. 2142–2151, 2013.

[31] Y. T. Tang, C. Panwisawas, J. N. Ghoussoub, Y. Gong, J. W. G. Clark, A. A. N. Németh, D. G. McCartney, and R. C. Reed, “Alloys-by-design: Application to new superalloys for additive manufacturing,” *Acta Materialia*, vol. 202, pp. 417–436, 2021.

[32] X. Wang, S. Sridar, and W. Xiong, “Thermodynamic investigation of new high-strength low-alloy steels with Heusler phase strengthening for welding and additive manufacturing: High-throughput

CALPHAD calculations and key experiments for database verification," *Journal of Phase Equilibria and Diffusion*, vol. 41, no. 6, pp. 804–818, 2020.

[33] S. Lin, C. Aliravci, and M. O. Pekguleryuz, "Hot-tear susceptibility of aluminum wrought alloys and the effect of grain refining," *Metallurgical and Materials Transactions*, vol. 38, no. 5, pp. 1056–1068, 2007.

[34] T. Kik, "Heat source models in numerical simulations of laser welding," *Materials*, vol. 13, no. 11, p. 2653, 2020.

[35] P. Promoppatum, S.-C. Yao, P. C. Pistorius, and A. D. Rollett, "A comprehensive comparison of the analytical and numerical prediction of the thermal history and solidification microstructure of Inconel 718 products made by laser powder-bed fusion," *Engineering*, vol. 3, no. 5, pp. 685–694, 2017.

[36] N. S. Shanmugam, G. Buvanashekaran, K. Sankaranarayanasamy, and S. Ramesh Kumar, "A transient finite element simulation of the temperature and bead profiles of T-Joint Laser Welds," *Materials & Design*, vol. 31, no. 9, pp. 4528–4542, 2010.

[37] S. M. Wasim and N. H. Zebouni, "Thermal conductivity of superconducting niobium," *Physical Review*, vol. 187, no. 2, pp. 539–548, 1969.

[38] C. M. Fischer, "Irreversibility field and critical current density as a function of heat treatment time and temperature for a pure niobium powder-in-tube Nb_3Sn conductor," *AIP Conference Proceedings*, 2002.

[39] F. Righini, R. B. Roberts, and A. Rosso, "Measurement of thermophysical properties by a pulse-heating method: Niobium in the range 1000-2500 K," *International Journal of Thermophysics*, vol. 6, no. 6, pp. 681–693, 1985.

[40] P. Kaur and C. Bera, "Effect of alloying on thermal conductivity and thermoelectric properties of CoAsS and CoSbS," *Physical Chemistry Chemical Physics*, vol. 19, no. 36, pp. 24928–24933, 2017.

CHAPTER 4

CONCLUSIONS

A summary of the conclusions is presented here along with recommendations for future work.

4.1 Conclusions

The hypothesis addressed by this study posits that single laser track melts in refractory alloys are representative of the microstructure in completed AM builds and show that LPBF laser conditions can be manipulated to create a tailored microstructure, which can be predicted by solidification models. The following questions were addressed in this study in response to the hypothesis.

1. *Can refractory alloy microstructures be controlled by laser conditions?*

   This study sought to understand the microstructure development during solidification in refractory alloys under AM conditions to develop guidelines for the AM conditions to achieve tailored microstructures. This was accomplished by evaluating the solidification behavior in single-track laser melts performed on refractory alloys and comparing these results to corresponding solidification models.

   This investigation was ultimately successful in showing that the melt pool morphologies and final microstructures can be manipulated by the laser parameters, indicating that tailored microstructures can be achieved by manipulating the laser parameters. The shape and size of each melt pool as it related to the processing parameters was consistent across all four alloys, though the grain morphology was not consistent. This information can be used in guiding future laser parameter selection. For instance, it can be concluded that melt track 2 (linear energy density: 1215 J/m) was too slow because it produced deleterious keyholing while melt tracks 4 and 5 (linear energy density: 238, 191 J/m) were too fast to produce ideal builds because they produced balling. Melt track 3 (linear energy density: 324 J/m) produced the most ideal behavior across alloys.

2. *Can the solidification behavior of refractory alloys under AM conditions be modeled?*

   This investigation showed that the material databases used capable of predicting general trends; the Schiel simulations aligned with EDS measurements, the non-equilibrium freezing range correlates with the relative total undercooling of each alloy, and the trends of the process maps aligned with the laser parameters used experimentally. However, the material databases ultimately proved insufficient when used to model the properties of these refractory alloys, demonstrated by the microstructure predictions not corresponding to experimental results. While the actual modeled values are unable to be validated with the currently available data for these materials, the likely changes in the values needed to create an accurate model were able to be predicted.

Therefore, the material property databases for refractory alloys, specifically as they relate to liquidus slope, partitioning coefficient, solid-liquid interfacial energies, and thermophysical properties, needs to be expanded to enable the development and calibration of accurate solidification models for these alloy systems.

3. *Is the behavior observed in a single-track representative of that observed in a completed build?*

   The behavior in the C103 track 3 (linear energy density: 324 J/m) was consistent with the behavior observed in the C103 AM sample (linear energy density: 311 J/m), which indicates that the evaluation of these single tracks can be applied to full builds. This evaluation of the single tracks in combination with the AM sample can thus be used to guide laser parameter selection; based on the AM parameters, it can be concluded that the parameters used for track 3 will produce similarly favorable results because both parameter sets have a similar linear energy density.

4.2 Recommendations for Future Work

1. This study evaluated alloy systems that are not critically assessed in Thermo-Calc. Experimentation and solidification modeling completed on a refractory system that is critically assessed would provide a valuable point of comparison for the evaluation completed in this study.
2. The material modeling in this study was only completed in Thermo-Calc. Similar modeling can also be completed with Pandat Software and compared to the results generated with Thermo-Calc.
3. Future single-track laser melt experimentation with refractory alloys should be completed with a preheat applied to the base material to mitigate cracking caused by the high hardness of the refractory alloys, specifically the Mo-containing alloys.
4. This study only evaluated BCC systems. It would be valuable to expand this analysis to other systems to further understanding of refractory systems.
5. A heat transfer model that accounts for convection in addition to conduction would likely more accurately simulate the temperature fields in melt track 2 and produce more consistent results. One such program is FLOW-3D, which not only takes convection into account, but is also capable of producing a more detailed model using a finer mesh.
6. The KGT model used in this analysis requires input parameters that are depended on both the overall alloy as well as the solute elements. The Gibbs-Thomson coefficient is alloy specific while the liquidus slopes, partitioning coefficients, diffusivities, and concentrations are all

specific to a solute element. For instance, in the Mo30Nb, these solute specific parameters were found and modeled for the Nb. However, the solute elements are less obvious for the equiatomic alloy, MoNbTaTi. This study assumed that the Ta was the “base” element while the Mo, Nb, and Ta were the solute elements because Ta has the highest melting temperature of the four elements and was therefore assumed to be the first element to solidify. However, each element’s contribution to total undercooling can also be considered when selecting the “base” element; it may also be valid to assign the element that contributes the least to the total undercooling as the “base” element. This avenue was not thoroughly explored in this study and should be explored further to ensure the accuracy of the solidification model.

7. The material property databases for refractory alloys, specifically as they relate to liquidus slope, partitioning coefficient, solid-liquid interfacial energies, and thermophysical properties, needs to be expanded. This is evidenced by Figure 2.7, in which the modeled thermal conductivity of C103 does not correspond to measured values. Further development of the currently available databases will enable the development and calibration of accurate solidification models for these alloy systems.

APPENDIX A

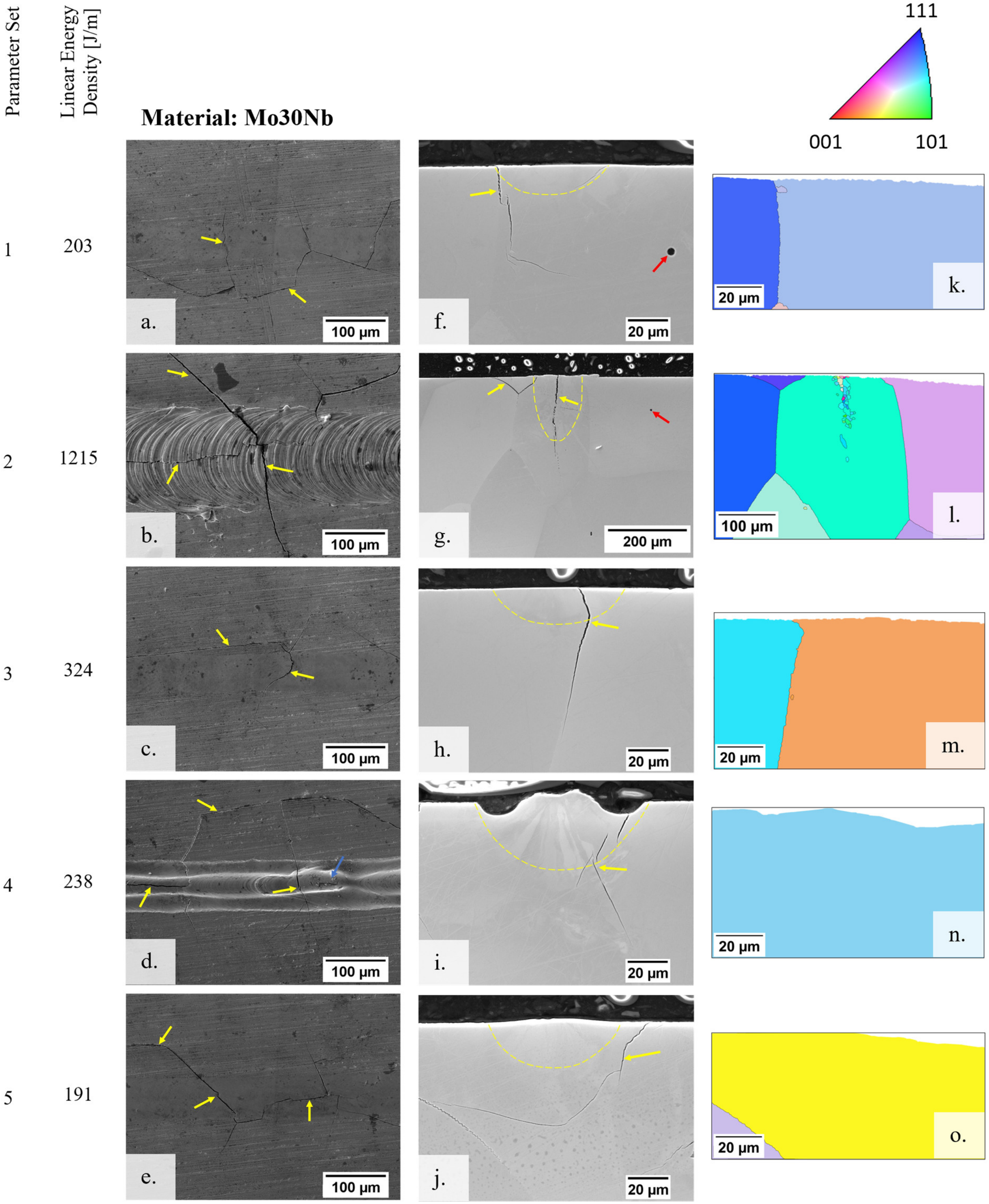

Figure A.1. Top-down images of each melt track on Mo30Nb are represented in a – e while the cross-sectional micrographs are shown in f – j. In these images, yellow arrows indicate cracking, red arrows indicate casting porosity, and blue arrows indicate balling. The IPF maps are shown in k – o with the corresponding laser parameters depicted to the left of the images and the IPF key is shown above the IPF maps.

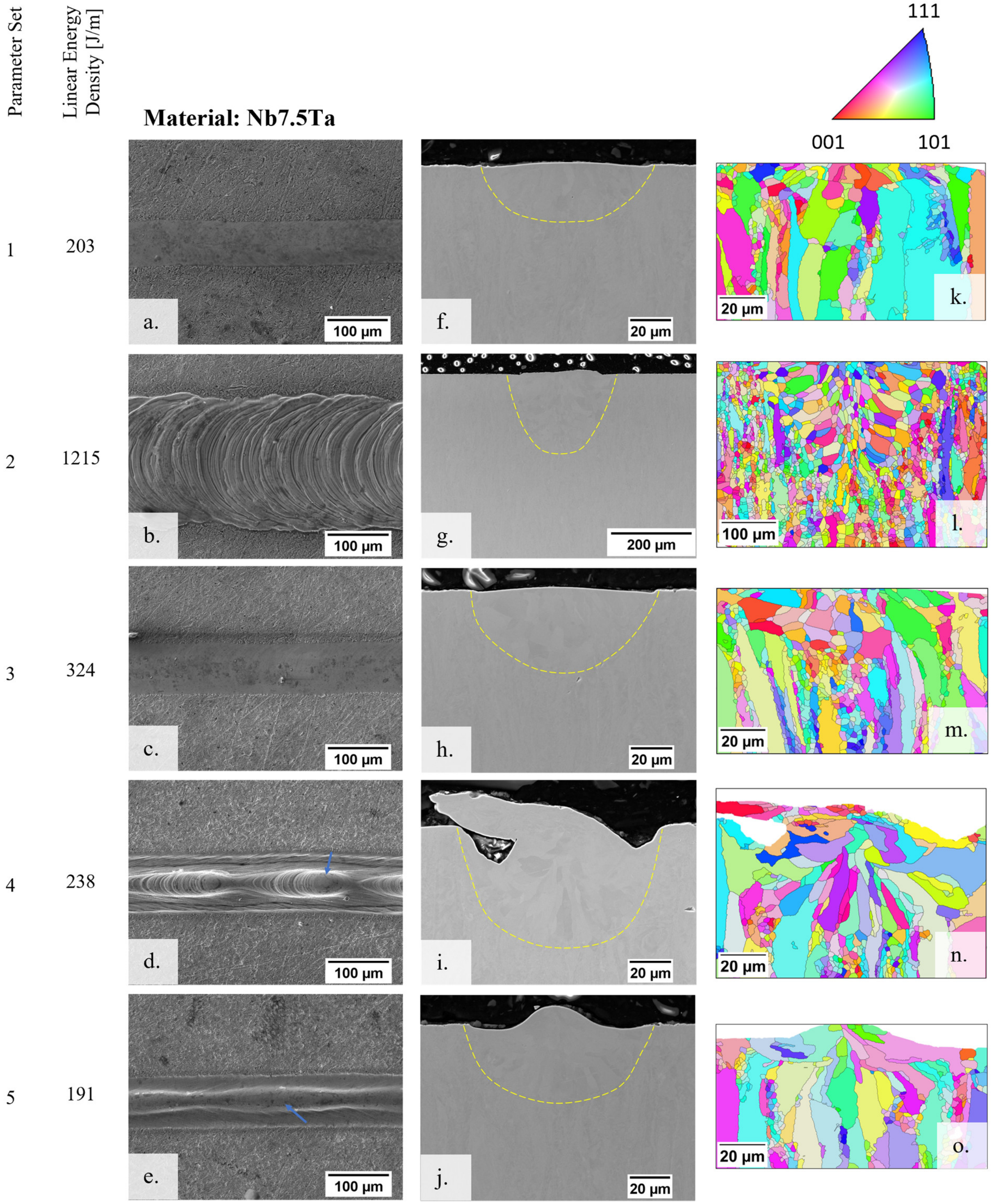

Figure A.2. Top-down images of each melt track on Nb7.5Ta are represented in a – e while the cross-sectional micrographs are shown in f – j. In these images, yellow arrows indicate cracking and blue arrows indicate balling. The IPF maps are shown in k – o with the corresponding laser parameters depicted to the left of the images and the IPF key is shown above the IPF maps.

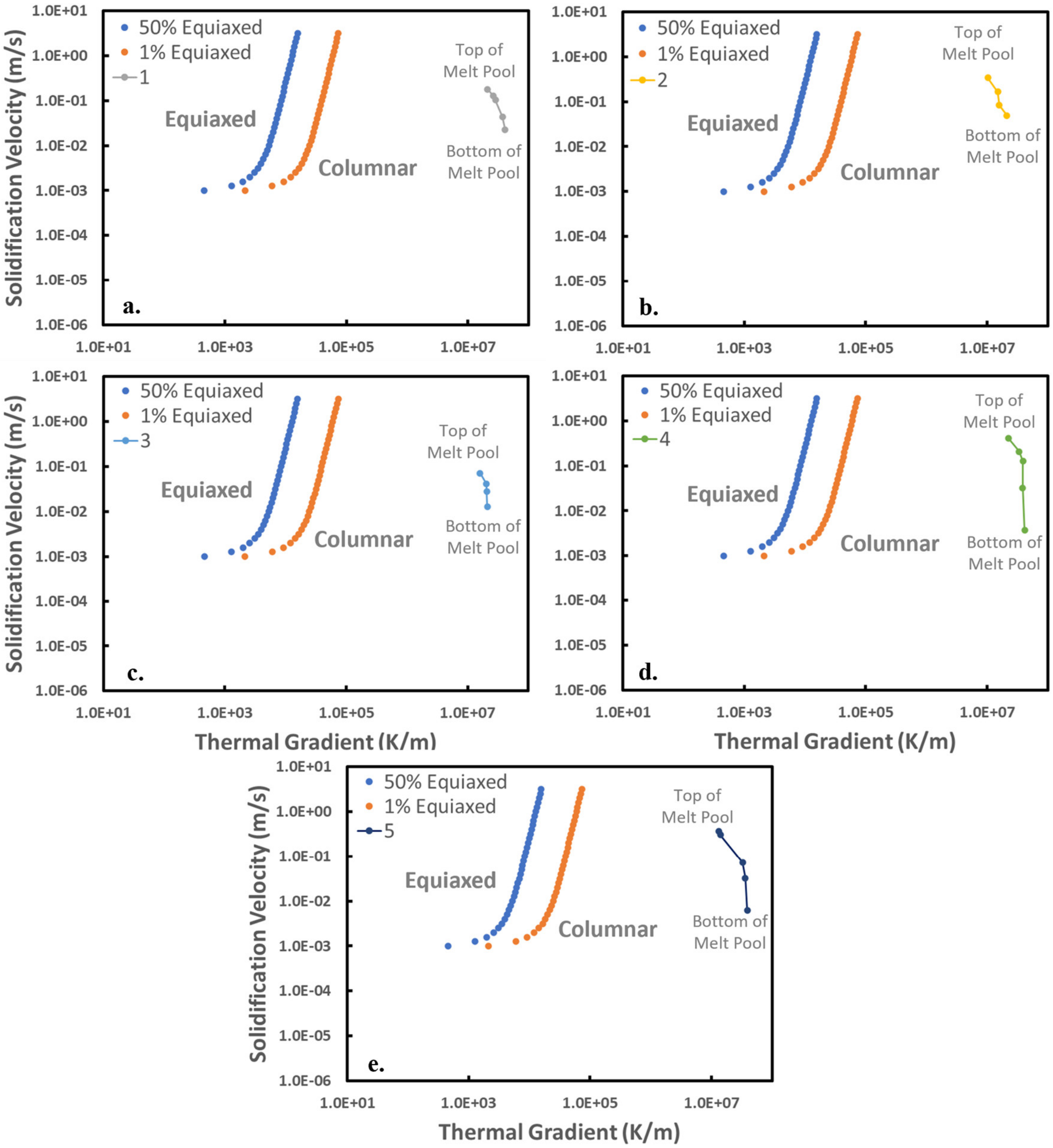

Figure A.3. Melt track-specific CET solidification maps for each track on Mo30Nb including the process maps for their respective melt tracks.

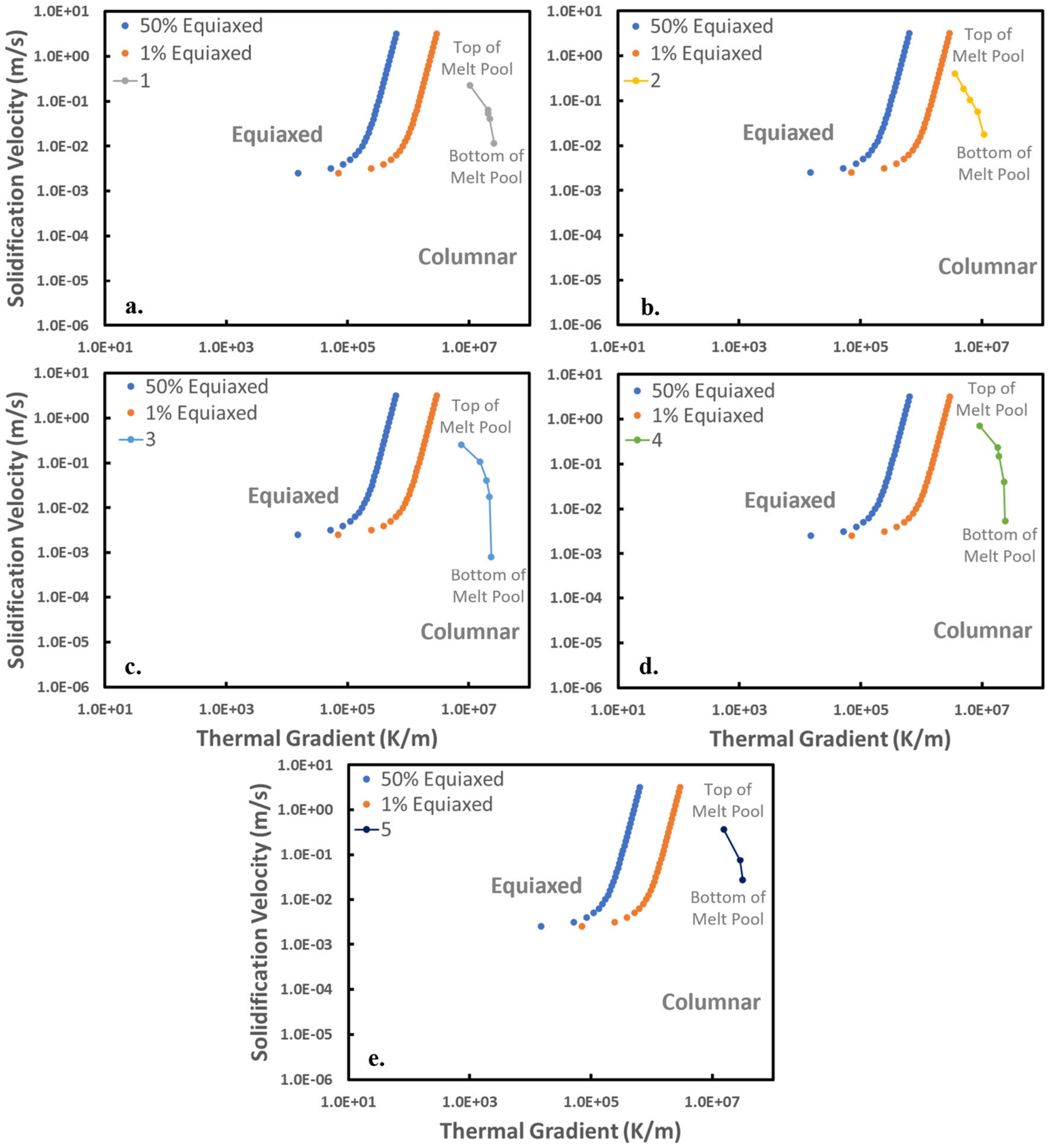

Figure A.4. Melt track-specific CET solidification maps for each track on Nb7.5Ta including the process maps for their respective melt tracks.